2019

Influence of Defects on the Stability and Hydrogen-Sorption Behavior of Mg-Based Hydrides

Grbović Novaković, J.; Novaković, N.; Kurko, S.; Milošević Govedarović, S.; Pantić, T.; Paskaš Mamula, B.; Batalović, K.; Radaković, J.; Rmuš, J.; Shelyapina, M.; Skryabina, N.

Published in:

ChemPhysChem

DOI:

10.1002/cphc.201801125

Document version:
Peer reviewed article (often known as postprint article)

A EUROPEAN JOURNAL

CHEMPHYSCHEM

OF CHEMICAL PHYSICS AND PHYSICAL CHEMISTRY

Accepted Article

Title: Influence of defects on Mg-based hydrides stability and hydrogen sorption behavior

Authors: Jasmina Grbovic Novakovic, Nikola Novaković, Sandra Kurko, Sanja Milošević Govedarović, Tijana Pantić, Bojana Paskaš Mamula, Katarina Batalović, Jana Radaković, Jelena Rmuš, Marina Shelyapina, Nataliya Skryabina, Particia de Rango, and Daniel Fruchart

To be cited as: *ChemPhysChem* 10.1002/cphc.201801125

Link to VoR: http://dx.doi.org/10.1002/cphc.201801125

A Journal of ChemPubSoc Europe

WILEY-VCH www.chemphyschem.org

10.1002/cphc.201801125

WILEY-VCH

Influence of defects on Mg-based hydrides stability and hydrogen sorption behavior

J. Grbović Novaković*[a], N. Novaković[a], S. Kurko[a], S. Milošević Govedarović[a], T. Pantić[a], B. Paskaš Mamula[a], K. Batalović[a], J. Radaković[a], J. Rmuš[a], M. Shelyapina[b], N. Skryabina[c], P. de Rango[d] and D. Fruchart[d]

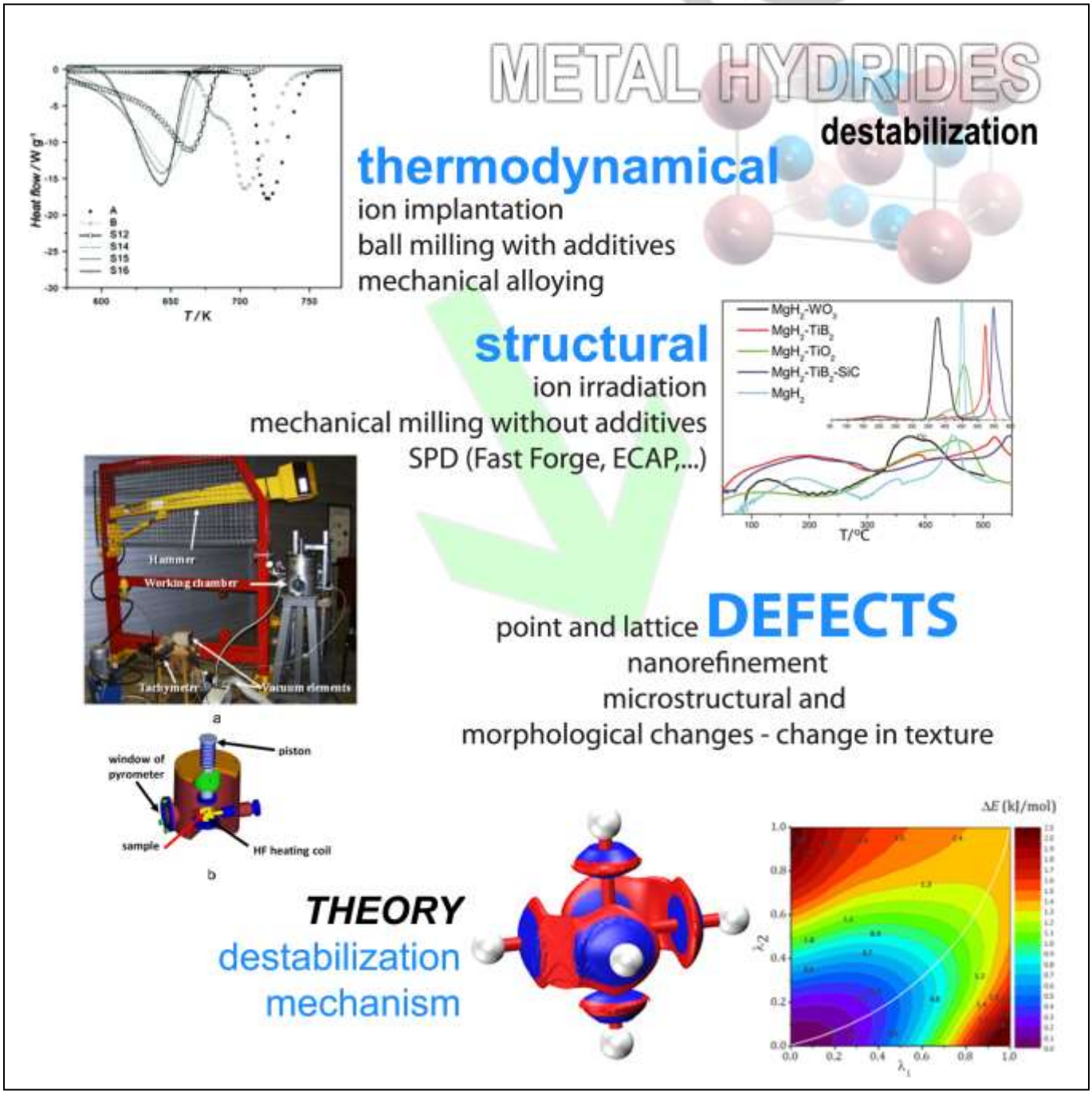

Abstract: This review deals with the destabilization methods for improvement of storage properties of metal hydrides. Both theoretical and experimental approaches were used to point out the influence of various types of defects on structure and stability of hydrides. As a case study, Mg, and Ni based hydrides has been investigated. Theoretical studies, mainly carried out within various implementations of DFT, are a powerful tool to study mostly MgH_2 based materials. By providing an insight on metal-hydrogen bonding that governs both thermodynamics and hydrogen kinetics, they allow us to describe phenomena to which experimental methods have a limited access or do not have it at all: to follow the hydrogen sorption reaction on a specific metal surface and hydrogen induced phase transformations, to describe structure of phase boundaries or to explain the impact of defects or various additives on MgH_2 stability and hydrogen sorption kinetics. In several cases theoretical calculations reveal themselves as being able to predict new properties of materials, including the ways to modify Mg or MgH_2 that would lead to better characteristics in terms of hydrogen storage. The influence of ion irradiation and mechanical milling with and without additives has been discussed. Ion irradiation is the way to introduce a well-defined concentration of defects (Frankel pairs) at the surface and sub-surface layers of a material. Defects at the surface play the main role in sorption reaction since they enhance the dissociation of hydrogen. On the other hand, ball-milling introduce defects through the entire sample volume, refine the structure and thus decrease the path for hydrogen diffusion. Two Severe Plastic Deformation techniques were used to better understand the hydrogenation/dehydrogenation kinetics of Mg- and Mg_2Ni-based alloys: Equal-Angular-Channel-Pressing and Fast-Forging. Successive ECAP passes leads to refinement of the microstructure of AZ31 ingots and to instalment therein of high densities of defects. Depending on mode, number and temperature of ECAP passes, the H-sorption kinetics have been improved satisfactorily without any additive for mass H-storage applications considering the relative speed of the shaping procedure. A qualitative understanding of the kinetic advanced principles has been built. Fast-Forging was used for a “quasi-instantaneous” synthesis of Mg/Mg_2Ni-based composites. Hydrogenation of the as-received almost bi-phased materials remains rather slow as generally observed elsewhere, whatever are multiple and different techniques used to deliver the composite alloys. However, our preliminary results suggest that a synergic hydrogenation / dehydrogenation process should assist hydrogen transfers from Mg/Mg_2Ni on one side to MgH_2/Mg_2NiH_4 on the other side via the rather stable a-$Mg_2NiH_{0.3}$, acting as in-situ catalyser.

[a] J. Grbović Novaković, N. Novaković, S. Kurko, S. Milošević Govedarović, T. Pantić, B. Paskaš Mamula, K. Batalović, J. Radaković, J. Rmuš
Center of Excelence for Hydrogen and Renewable Energy CONVINCE
University of Belgrade, Vinča Institute of Nuclear Sciences
POB 522, 11001 Belgrade, Serbia
E-mail: jasnag@vin.bg.ac.rs

[b] M. Shelyapina
Department of Nuclear Physics Research Methods
Saint Petersburg State University
7/9 Universitetskaya nab., St. Petersburg 199034, Russia

[c] N. Skryabina
Department of Physics
Perm State University
Bukireva street, 15.Perm 614990, Russia

[d] P. de Rango, D. Fruchart
Institute Néel, CNRS
Grenoble, France

Jasmina Grbović Novaković - Graduate degree in physical chemistry,1999, Magisterium in physical chemistry, 2003, PhD in physical chemistry 2005. President of Serbian Society for Microscopy from 2010-2014. 2009 awarded from International Association of Hydrogen Energy with IJHE outstanding Service Award. Guest Editor: Novel Perspectives on Hydrogen Storage in Solid Media and International Journal of Hydrogen Energy. From 2018 she is the head of Centre of excellence for hydrogen and renewable energy at Vinca Institute.

Nikola Novaković (PhD in Physics), His research interests include theoretical modelling of various metal-hydrogen solid and molecular systems (electronic structure calculations using state-of-art WIEN2k, Abinit. CPMD, Crystal and VASP codes) and local structures investigation of various semiconducting systems

Dr. **Sandra Kurko** received her B.Sc. from the Faculty of Physical Chemistry at University of Belgrade (Serbia) in 2008, and her Ph.D. from the same university in 2015. Her research interests include Solid state hydrogen storage, DFT calculations, Photocatalytic materials for hydrogen production, Ion irradiation.

Sanja Milošević Govedarović (PhD in Physical Chemistry). Her research area covers various materials for solid state hydrogen storage and electrode materials for Li-ion batteries. Her presentations at international events were noticed and rewarded.

Tijana Pantić received her BSc from the Faculty of Physical Chemistry, University of Belgrade (Serbia) in 2014, and her MSc from the same university at 2016. Her research interest include composite materials for solid state hydrogen storage.

Dr. **Bojana Paskaš Mamula** attended the Faculty of Physics, University of Belgrade (Serbia) and received her B.Sc. in 2005. She completed her doctoral dissertation in 2017. The field of her scientific research is DFT based theoretical modeling of different hydrogen storage systems with emphasis on investigating the charge density with the Quantum Chemical Topology methods.

Dr. **Katarina Batalović** received her M.Sc. from Faculty of Physical Chemistry, University of Belgrade (Serbia) in 2008 and her Ph.D. from the same University in 2013.. Her research interests include hydrogen storage, photocatalytic hydrogen production, quantum chemistry and materials design. In 2009. she received "Pavle Savić" award from Society of Physical Chemists of Serbia.

Dr. **Jana Radaković** received her Diploma degree from the Faculty of Physical Chemistry, University of Belgrade (Serbia) in 2008, and her PhD from the same university in 2013 Her research interests include Computational materials science in renewable energy and energy storage development.

Jelena Rmuš is a Ph.D. student at the Faculty of Physical Chemistry, University of Belgrade (Serbia) since October 2017. She finished her M.Sc. in 2017, and her B.Sc. in 2016 at the same Faculty. Her doctoral research is focused on nanomaterials for hydrogen energy and the application of hydrogen as a renewable energy source, particularly on synthesis and characterisation of nano and two-dimensional transition metal chalcogenides.

Prof. **Marina Shelyapina** received her M.Sc. from Saint Petersburg State University (Russia) in 1995, and her Ph.D. from the same university in 2000 with Prof. V. Kasperovich. After post-doctoral research in the lab of Prof. D. Fruchart (Neel Institute, National Center for Scientific Research, France), she accepted a position as Assistant Professor at Saint Petersburg State University in 2004. Her research interests include Solid State NMR, DFT Calculations, Metal-Hydrogen Systems, and Composite Nanomaterials.

Nataliya Skryabina - Master Perm State Univ. 1979. PhD Polytech. Inst. Voronezh 1987. Hab Thesis, Perm State Univ. 1999.Full State Professor at Perm State Univ. 2000. Corresp. Member of Russian Academy Natural Sciences 2004. Main scientific research interests: Fundamentals of Metal-Hydrogen systems (structure, physics, thermodynamics & mechanics of M-H interactions). Applied properties (reversible storage). Shape Memory Materials, Electrochemistry. Electron Microscopy, Methods of SPD. Synthesis and metallurgy of crystal, nanocrystalline and non-ordered materials.

Patricia de Rango (PhD in Physical Chemistry) from the University J. Fourier, Grenoble. From '92, she got a permanent position at CNRS, to study rare-earth compounds and permanent magnets. She applied hydrogen processes to synthesis highly coercive and anisotropic powders for bounded magnets by in-situ neutron scattering, thermomagnetic measurements and EXAFs. Since 2002 she works on metal hydrogen storage and the investigation of the hydrogenation mechanisms to the development of instrumented tanks, including analyses of heat and mass transfers during hydrogenation and dehydrogenation steps. She is the author of more than 80 referred journal articles and 10 issued patents. She is an expert member at the IAE.

Daniel FRUCHART- Master Fund. Mathematics 67 Univ. Lille.Master Phys. & Crystal. 69 Univ. Grenoble. PhD Thesis 71, State Hab Thesis 76. Research Director, Institut Néel CNRS 84-09, Emeritus Res. Dir. 10-20. Head CNRS Research Team (12 staffs) 82-09. Head of French-Spanish European Lab. MANES 98-02. Co-Founder & Res. Manager, McPhy Energy 08-13. Major Awards: 1-French Division of Chem. & Metal.-86, 2-Innov. Techn. for Environ. & Energy-04, 3-French Phys. Soc.-12. Chair Physics State Committee, LURE Synchrotron

99-03. Board National Committee Neutron Scattering 98-00. Interests: Magnetic materials, M-H systems, Metallurgy Interstitials & Intermetallics, Thin films, Neutron scatter. & X-ray spectroscopies.

1. Introduction

Fuel cells and other systems for hydrogen energy utilization are promising alternatives in today's fossil fuels driven economy [1]. However, for their practical applications some problems concerning efficiency and safety need to be solved, with hydrogen storage not being the least of all. Hydrogen is one of the promising alternatives to fossil fuels, while it is frequently referenced as an energy vector rather than a fuel. It has a very high mass energy density (around 120 MJ/kg, compared to i.e. 48 MJ/kg for gasoline) [2]. Unfortunately, it also has a very low volumetric energy density, due to its lightness in the molecular form. Hydrogen is conventionally stored in high pressure hydrogen-durable steel or composite tanks, or in liquid form in cryogenic conditions. Due to its high flammability in wide range of mixing ratio with air oxygen, the storage in high pressurized gaseous or liquid form remains a potential security issue.

Hydrogen storage materials with high gravimetric and volumetric capacities are, on the other hand, easily available, cheap, safe and a non-toxic alternative [1]. In solid-state storage materials, hydrogen is bonded by either physical (H_2 is physisorbed on the surface of the pores) or chemical forces (H is bonded with medium) [3]. The advantages of metal-organic frameworks, porous carbons, zeolites, clathrates, and organic polymers which belong to the class of physisorption materials have a high specific surface area and the possibility of tailoring the pore dimensions [4-10]. The main drawback of those classes of materials is that high storage capacity is reached at the liquid nitrogen temperature and high pressures [4]. At the ambient temperature and pressure their capacities become very low. On the other hand, in aminoboranes [11, 12], borohydrides [13,14] and metal hydrides [15-17] hydrogen is chemically bonded to the storage medium. Due to relatively high activation energy, the sorption in such kind of materials is usually not reversible.

The subjects of the investigations presented in this review are Mg, Zr and Ni based hydrides. These are the typical representatives of simple metal and interstitial metal hydrides, with prospect of possible economic viability.

Among metal hydrides, magnesium hydride (MgH_2) stands out as promising hydrogen-storage material, due to its lightness, availability, low cost and non-toxicity. It has very high gravimetric density (7.6 wt%). The major obstacle to economic viability of this material remains its high desorption temperature and sluggish kinetics. Both of mentioned properties are derived from MgH_2 being simply 'too stable'. Its heat of formation (around 76 kJ/molH_2) is responsible for the very high desorption temperature at normal conditions (around 300 °C), while there are numerous proposed mechanisms responsible for slow desorption / absorption kinetics.

The common approach to the abovementioned problems is to destabilize the host structure by means of nanostructuring or various single or collective defects introduction (vacancies or dopants, metals, metal oxides, halides, nonmetals etc.), composites using mechanosynthesis or ion irradiation implantation, etc. On the other hand, Mg_2NiH_4 is an attractive material for hydrogen storage due to favorable hydrogen to metal weight ratio of 3.6 wt%. Even though the lower enthalpy of dissociation of Mg_2NiH_4 (64 kJ/mol H_2) in comparison to MgH_2 results in a lower decomposition temperature for the same hydrogen external pressure, the main drawback of this material is its inability to be fully recharged with hydrogen. As reported by Révész *et al.,* upon cycling at low hydrogen pressure, Mg2Ni can absorb hydrogen (at T_{peak}= 247 °C, at 300 kPa H_2) only to form the partial hydrogenated hexagonal solid solution $Mg_2NiH_{0.3}$ [18,19].

The subject of this paper are possible paths of destabilization of Mg-based metal hydride systems by defects introduction, in order to 1) obtain improved H (de)sorption properties and 2) to investigate the mechanisms of the processes responsible for slow kinetics and high desorption temperatures.

We are reporting here combined theoretical and experimental approach for treatment of various defects introduction (neutral and charged vacancies, displaced atoms of host lattice and substitutional and interstitial dopants). The experimental methods for synthesis and modification of materials include mechanosynthesis, ion irradiation, ECAP and Fast-Forging. For theoretical description of induced changes, the various calculation methods were used, such as DFT based pseudopotential and linear all-electron methods applied on cluster, bulk, surface, single interface and multilayer models. The structure of the review paper reflects mentioned methods and its results.

2. Experimental approach to destabilization of hydrogen storage materials

2.1 Ion irradiation as a method for hydride structural destabilization

Ion-beams processing of materials provides new opportunities for synthesizing materials with unique microstructures and properties. It is clear that ion irradiation is not the most convenient method to improve properties of materials on industrial scale or in terms of hydrogenation cycling. The idea behind the investigation of ion irradiation as a mean of defects production in Mg-based hydrides is to investigate the role of surface and near-surface regions as sources of suspected rate limiting steps during sluggish (de)sorption. The expected role of low energy light and heavy ions is to deposit defects (vacancies, recoils, interstitials) in a well-defined depth range close to surface, as predicted by simulations, and to investigate the impact of different mechanisms of ion-target interaction based

on energy-loss mechanism (projectile nature, weight, charge state and initial energy).

Interaction of incident ions and solid involves series of collisions with both the electrons and the ion cores of target atoms. Inelastic collisions of ions with electrons lead only to deceleration of incident ions, since electron mass is small and doesn't alter the ion trajectory much. So, electrons in target can be treated as viscous, energy extracting background [20]. The energy loss of ions by inelastic collisions with target electrons is electronic stopping power $S_e(E)$ and it depends on the target atom's mass and incident ion's mass and energy. On the other hand, collisions of incident ions with the ion cores of target atoms are elastic and can lead to atomic displacement whereby a knocked-on atom recoils away from its initial lattice site and produces an interstitial-vacancy (Frenkel) pair. To form stable Frenkel pairs, target atoms need energy of ≈25 keV. When received more energy, these recoils can develop displacement cascade with more target atoms displaced. Energy loss induced by these interactions is nuclear stopping power $S_n(E)$. Interaction of ions with surface and near-surface target atoms can lead to their sputtering and erosion of material surface. Partial sputtering yields are different, so the surface composition becomes altered from the bulk composition [21,22]. In alloys, the displacement process induced upon ion irradiation leads to ion mixing since a portion of atoms in the vicinity of the recoils exchange lattice sites with neighboring atoms. The displacement cascade lasts for a few tenths of ps and the local temperature usually exceeds the melting temperature for few ps. This causes a liquid-like diffusion and induces defects clustering upon the system cooling [23]. Around the incident ion track, a region of disorder is produced. With the increase of ion fluence, the disorder increases and disordered zones are formed, until all the atoms have been displaced and an amorphous layer is produced over a region (see figure 1). The amorphization takes place when the material reaches a critical threshold in the defect density. The threshold fluence for amorphization increases with increasing the target temperature up to a critical value, above which amorphization does not happen. The critical temperature depends on the ion mass and energy, i.e. on the energy density deposited into nuclear collisions.

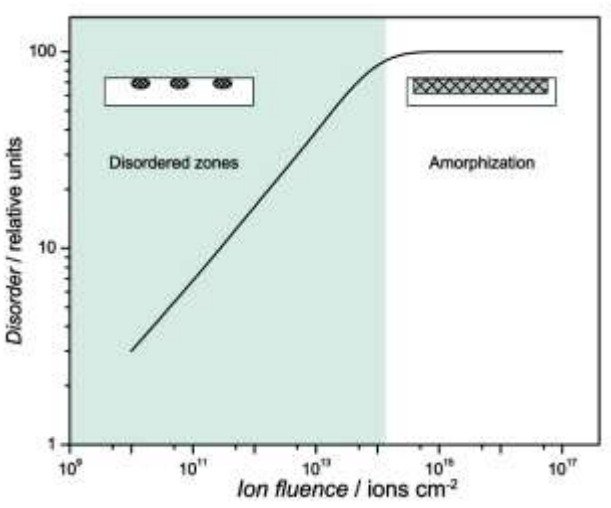

Figure 1. Disorder accumulation as a function of ion fluence

Ion irradiation method found a significant application in the structural destabilization of materials for solid state hydrogen storage [15-17,24-37]. This way it is possible to introduce a well-defined concentration of defects (vacancies and dislocations) in the surface and subsurface layer of material. [24,24]. Surface modification is crucial for hydrogen reactivity with the material, since the H_2 gas molecule dissociation is the first step in the hydrogen absorption reaction [17].

Abe *et al.* showed that hydrogen absorption of palladium can effectively be improved by ion bombardment [11]. They used low energy ions (30-350 keV) of H^+, He^+, N^+ i Ar^+ with the fluence range between 10^{14}-10^{17} ions/cm^2. Irradiation introduced vacancies, dislocations and micro cracks into materials and increased the rate of hydrogen absorption. The absorption rate was proportional to the ion fluence and energy of used ions. The highest effect was produced by nitrogen ions [25]. They also studied the irradiation effect that various ions have on the initial reaction rate of hydrogen absorption in electrode materials for Ni-H and NiM-H batteries based on rare earth based alloys [27-29]. $MmNi_{3.48}Co_{0.73}Mn_{0.45}Al_{0.34}$ ($Mm=La_{0.35}Ce_{0.65}$), which is applied as the negative electrode of the Ni–H batteries and other hydrogen storage systems, was irradiated with H^+, Ar^+ i K^+ ions of 350 keV energy, while fluence ranged from 10^{14} ion/cm^2 to 10^{17} ion/cm^2 [27]. Irradiation with Ar^+ ions increased the initial hydrogenation rate more than irradiation with H^+ ions. This was attributed to the higher concentration of vacancies induced by Ar^+ ions and consequently larger number of active sites for hydrogen adsorption on the alloy surface. As a result, nucleation and hydride phase growth are accelerated. On the other hand irradiation with K^+ ions was found to be more effective than Ar^+ ions. This phenomenon was connected to the possibility of K^+ chemical interaction with alloy in the surface layer, in addition to the vacancy introduction. In all experiments initial hydrogenation rate increase was directly proportional to the fluence of incident ions. It was also shown that surface modifications with 350 keV

lanthanum (La^+) and cerium (Ce^+) ions combined with an alkaline KOH treatment are much more effective in the enhancement of the initial hydrogenation rate and have the synergic effects on the surface modification [28]. On the other hand, no such effect was observed for Mg^+ and Bi^+ ions of the same energy. The reason is the concentration and depth distribution of produced vacancies. La^+ and Ce^+ ions introduce high concentration of vacancies (over 10^{24} cm^{-3}) in the subsurface layer of alloy up to the depth of 200 nm. The similar ion depth distribution is calculated also for Bi^+ ions. The absence of improvement in this case leads to conclusion that the nucleation and growth of hydride phase are not only influenced by the vacancies acting as the H trapping sites but also by the ions remaining in or near the formed defects since La and Ce tend to form stable hydrides [29]. High concentrations of the vacancies near the alloy surface accelerate also the oxidation and alloy reaction with air moisture, so the alkaline treatment leads to penetration of alkaline atoms in the freshly formed surface oxide layers and reduction in the work function of surface electrons, resulting in the improvement of H_2O dissociation and consequently hydrogenation [30,31]. The importance of material surface and vacancies depth distribution was also confirmed in irradiation experiments of $LaNi_{4.6}Al_{0.4}$ with O^+ ions of different energies [31].

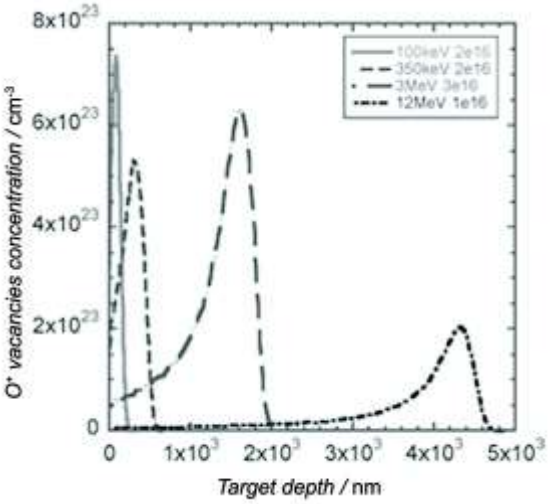

Figure 2. Vacancy depth distributions in the $LaNi_{4.6}Al_{0.4}$ alloy induced by O^+ irradiation of different energies using a SRIM code. Reproduced with permission from H. Abe, S. Tokuhira, H. Uchida, T. Ohshima, Nucl. Instrum. Methods Phys. Res., 2015, B 365, 214.[31].

In Figure 2 vacancies depth distributions are shown, induced by irradiation using ions of different energies obtained by Monte Carlo simulations using SRIM code [32]. In the alloy irradiated with 100 keV and 350 keV O^+ ions, the initial hydrogenation rate was improved by two orders of magnitude while in the case of 3 MeV and 12 MeV ion energies rate was similar to the un-irradiated material (table 1). The amount of absorbed hydrogen was also significantly enlarged in the alloys irradiated with low energy ions. The difference in material properties irradiated with different ion energies was attributed to the difference in depth distribution and concentration of produced vacancies.

Table 1. The initial rate of hydrogenation, amount of hydrogen absorbed and linear energy transfer for different ion beam energies used to irradiate $LaNi_{4.6}Al_{0.4}$. Reproduced with permission from H. Abe, S. Tokuhira, H. Uchida, T. Ohshima, Nucl. Instrum. Methods Phys. Res., 2015, B 365, 214 [31].

Ion beam Energy	Initial rate of hydriding: (r/min^{-1})	Amount of hydrogen absorption: ($\Delta X /HM^{-1}$)	LET (Linear energy transfer) ($keV/mg^{-1}cm^2$)
Un-irradiated	$3.52x10^{-3}$	0.267	
100 keV	$3.35 x10^{-1}$	1.89	$7.29x10^2$
350 keV	$1.89 x10^{-1}$	1.28	$1.80 x10^3$
3 MeV	$3.42 x10^{-3}$	0.393	$3.56 x10^3$
12 MeV	$2.98 x10^{-3}$	0.230	$4.26 x10^3$

López-Suárez *et al.* [33] have studied hydrogen absorption and diffusion into H^+ irradiated titanium. They used low energy (5 keV) hydrogen ions at a fluence of 10^{14} ions/cm^2 with the calculated ion projected range of 64 nm. The experimental hydrogen depth profile obtained by ERDA is slightly wider than in the SRIM simulation and the projected ion range is 81 nm, which suggests that radiation induced hydrogen diffusion into bulk is taking place during the implantation. Hydrogen absorption in irradiated samples was significantly improved. Un-irradiated Ti absorbs hydrogen at temperatures higher than 550 ^oC; in the irradiated samples absorption is notable even at 300 ^oC, while it becomes significant at 450 ^oC. Also, there is an important increase in the quantity of absorbed hydrogen at all studied temperatures. The improvement was attributed to the change in both strain and structure in the surface region that enhances the defects and dislocations creation leading to the formation of pathways for hydrogen's easier diffusion into metal.

Our group systematically studied the influence of low energy irradiation effect of different ions on MgH_2 dehydrogenation reaction and its correlation to the irradiation induced changes in the hydride structure [15,16,34-37]. The used ions, their energies, the position of maximum of ions range and number of produced vacancies per ion calculated by SRIM [32] are represented in Table 2. Fluences of used ions were in the range from 10^{12} ions/cm^2 to 10^{16} ions/cm^2.

The heavier ions Ar^{8+} and Xe^{8+} produced larger concentration of vacancies than lighter ions B^{3+}, N^{3+} and C^{2+}. Vacancies produced by Xe^{8+} ions are deposited closer to the surface. The maximum of vacancies production corresponds to the maximum of the recoil atoms distribution since recoils produce about eight times more vacancies than incident ions and is positioned at the depth of about 54 nm [16]. High concentration and shallow deposition of vacancies produced by Xe^{8+} ions led to significant decrease in hydrogen desorption maxima in MgH_2 (Figure 3)

Table 2. Type of Ions, their energies, main ions range and number of produced vacancies per ion, as calculated by SRIM used for irradiation of $_2$ in [15,16,34-37].

Type of ion	Ion energy (keV)	Ions range maximum position (nm)	Ion range FWHM (nm)	Number of vacancies created per ion
Ar^{8+}	120	175	60.0	1244
Xe^{8+}	120	85	103.0	1818
B^{3+}	45	216	93.0	288
N^{3+}	45	170	90.0	359
C^{2+}	30	140	78.5	259

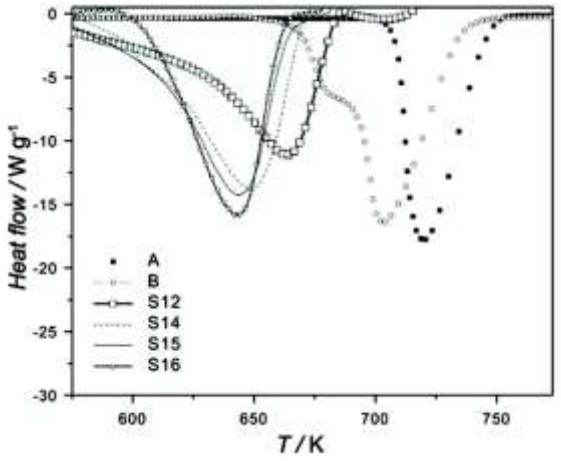

Figure 3. DSC curves of commercial MgH_2 powder (A), MgH_2 milled for 10 h (B), and MgH_2 irradiated by 120 keV Xe^{8+} with ion fluences: 10^{12} (S12), 10^{14} (S14), 10^{15} (S15), and 10^{16} (S16) ions cm^{-2}. Reproduced with permission from J. Grbović Novaković, Lj. Matović, M. Drvendžija, N. Novaković, D. Rajnović, M. Šiljegović, Z. Kačarević Popović, S. Milovanović, and N. Ivanović, Int. J. Hydrogen Energy, 2008, 33, 1876 [16].

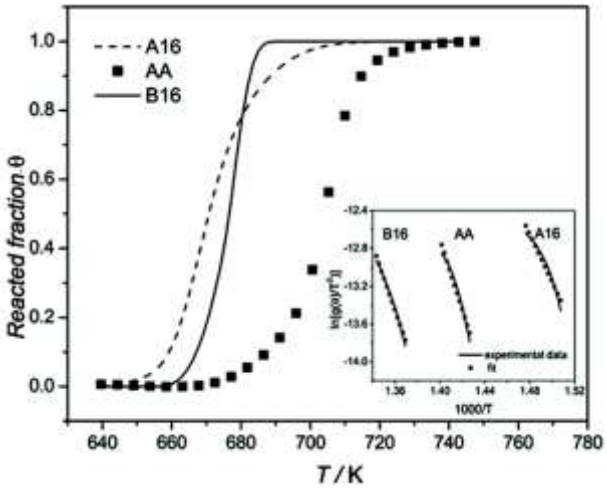

Figure 4. Temperature evolution of reacted fraction θ corresponding to MgH_2 decomposition, obtained by integration of high temperature TPD peak in MgH_2 (AA), and MgH_2 irradiated with 10^{16} ions/cm^2 Ar^{8+} (A16) and B^{3+} (B16) ions. Reproduced with permission from Lj. Matović, S. Kurko, Ž. Rašković-Lovre, R. Vujasin, I. Milanović, S. Milošević, J. Grbović Novaković, Int. J. Hydrogen Energy 2012, 37, 6727 [37].

It is noticeable that ball milling, as a form of bulk modification, induced lower decrease in desorption temperature than surface modification induced by Xe^{8+} ion irradiation. The increase of ion fluence in irradiated samples was followed by the change in DSC peaks shape that became more symmetric and narrow. The more symmetrical peak indicates only one process that limits H desorption kinetics, while the DSC peak asymmetry at lower fluences is an indicator of multiple steps that control hydride dehydrogenation. There is also a dependence of peak position on ion fluence, so the higher is the fluence and related vacancy concentration in the sample, the lower hydrogen desorption temperature is. Besides the effect of catalytically active vacancies, the improvement in reaction kinetics is also attributed to the disruption of Mg-oxide passivation surface layer. Obtained results showed that there is a direct correlation of decrease in hydrogen desorption temperature to the concentration and position of created vacancies (Table 2), so it increases in the following order $T_{des}(Xe^{8+}) < T_{des}(Ar^{8+}) < T_{des}(N^{3+}) < T_{des}(B^{3+}) < T_{des}(C^{2+})$ [15,15,34-37]. In the case of C^{2+} a large concentration of $Mg(OH)_2$ formed upon irradiation so the hydrogen temperature increased upon passivation of surface [36]. In Ar^{8+} and B^{3+} irradiated hydride, the hydrogen desorption temperature and reaction mechanism is independent on the ion fluence, so it led to an assumption that the irradiation induced defect network for H-diffusion was already formed in the sample irradiated with the lowest fluence (10^{12} ions/cm^2) [15]. Comparison in dehydrogenation reaction mechanism between MgH_2 irradiated with B^{3+} and Ar^{8+} ions indicated that it is dependable on vacancy depth distribution (figure 4) [37]. The Avrami-Erofeev parameter changed from n=3 in B^{3+} irradiated hydride to n=2 in the case of Ar^{8+} ions, as a consequence of change in nucleus growth dimensionality from 3D to 2D.

Further clarification in 2D reaction mechanism in Ar^{8+} irradiated MgH_2 was studied in the MgH_2 thin films [38]. In the non-irradiated MgH_2 thin film hydrogen desorbs at 447ºC and the peak is asymmetric. On the other hand, in the irradiated sample, the nuclei, once formed, grow continuously, resulting in a symmetric, broad TDS peak at a lower temperature. Reaction kinetics is drastically improved upon irradiation. While in non-irradiated film full hydrogen desorption finishes in 2000 s, in irradiated sample it finishes within 200 s (Figure 5). The Avrami parameter is changed from 4.1 in non-irradiated to 2.5 in irradiated films, with the lowering in activation energy for hydrogen desorption from 319 kJ/mol H_2 to 137 kJ/mol H_2 upon irradiation.

The value 2.5 of Avrami parameter is attributed to the high number of induced defects in the material. The irradiated film had a significantly different microstructure than non-irradiated films, dominated by large crystal grains embedded in a crystallite matrix. The kinetics of the irradiated film is faster even though

the crystallites are larger. This was attributed to sample inhomogeneity, severe microstructural changes in the surface-top region and the fact that large number of vacancies (about 760 vacancies per incident ion), led to formation of H-deficient phases. In the non-irradiated film the random nucleation of spherical Mg nuclei is observed and the simultaneous growth of small and big nuclei. On the other hand, in irradiated one irregularly shaped nuclei are found and the nucleation process in this sample is very fast due to clustering of the Mg nuclei along preferential directions determined by the vacancy distribution.

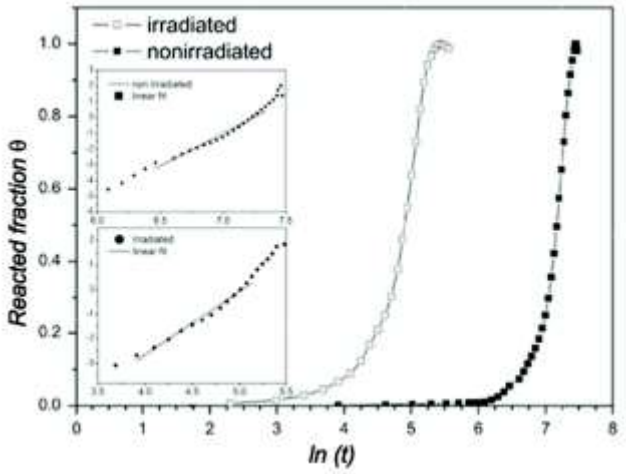

Figure 5. Hydrogen desorption curves from isothermal measurements (at 400ºC, coverage-surface area vs. time) for irradiated and non-irradiated 300 nm thick MgH_2 thin films. Reproduced with permission from Ž. Rašković Lovre, S. Kurko, N. Ivanović, J. F. Fernandez, J. R. Ares, S. Šturm, T. Mongstad, N. Novaković, J. Grbović Novaković, J. Alloys and Compd, 2017, 695, 2381-2388 [38].

Ion irradiation is a very useful method for introduction of controlled concentration and depth distribution of defects into surface and near-surface area of hydrides. Highly disordered surface of material, reach in catalytically active point defects leads to improvement of hydrogen reactivity with hydrogen storage materials and their overall performance.

2.2 Oxide and non-oxide ceramics addition as a method for hydride structural destabilization

Methods like ion bombardment and mechanical milling [39-43] were often used to modify materials to facilitate diffusion. Mechanical milling is a very convenient method because it is both fast and simple for the particle/grain size reduction and even for an alloying of two or more metals [44]. Another effect that can be induced in single-phase material by mechanical milling is the loss of long-range order, while prolonged milling can lead to an amorphous state. Depending on the design, capacity, efficiency of milling, and other arrangements, we distinguish several types of mills: SPEX shaker mill, planetary ball mill, attritor mills and high capacity commercial mills such as horizontal rotary ball mill, Uni-ball mills, etc. Depending on the type of mill, different energy transfers to the powder are obtained: impact, shear modes, or a combination of both. Other than on types of mill, the milling results are also dependent on other milling variables such as milling energy / speed, milling time, Ball-to-Powder Weight Ratio, milling atmosphere, milling container, types of milling balls, temperature of milling, and of course, properties of milled powder [44]. Prolonged milling in high-energy ball mill (for example 20 hin Spex 8000 [45]) can lead to change of crystal cell parameters of powders and to amorphization of crystalline material. If amorphization or alloying is not the desired outcome, the milling time should be shorter and properly set. On the other hand, if milling is performed in a planetary mill such as Fritsch Pulverisette 5 for example, long-term milling (100 h) leads to a point where agglomeration and size reduction become competitive and opposed processes, and further milling doesn't reduce particle size [46], so it is important to find optimal conditions.

Table 3. List of commercial and MgH_2 powders obtained from different manufacturers and milled MgH_2 powders, their particle size and desorption temperatures obtained by DSC. Multiple temperatures correspond to multiple DSC peaks.

Ref.	**Com. MgH_2** Manufact., PSD	**Com.MgH_2** DSC T_{des}(°C) /**rate** (°C/min)	**Milled MgH_2** Milling time (h) / **Particle size**(nm)	**Milled MgH_2** DSC T_{des} (°C) /**rate** (°C/min)
[47]	*Alfa Aesar*, 98%, >100 nm	459 / **10**	0,3 / **11**	371 / **10**
[48]	*Alfa Aesar*, 98%, ~70 µm	/	20 / **150-3000** (by SEM)	380, 466 / **5**
[42]	*Tego Magnan*, ~95%, 36 µm	415 / **4**	0,25 / **2032** 1 / **956** 10 / **470** 25 / **1310** 50 / **1184** 75 / **839** 100 / **600** (by SEM)	404 / **4** 372, 395 / **4** 362, 381 / **4** 389, 407 / **4** 379, 395 / **4** 376, 386 / **4** 365, 380 / **4**
[49]	*Gold Schmidt AG*, 95%	414 / **5**	200 / **250–5000 (max at 900)**	323, 354 / **5**
[50]	*ABCR Germany*, 98%	~445 / **20**	20 / **8000**	368 / **5** 381 / **10** 397 / **20**
[51]	*Gold Schmidt AG*, 95%, 20–60 µm	414 / **5**	100 / **?**	336 / **5**

It is known that the hardness of material plays a significant role and can contribute to the grinding of powder. If hard powder is used as an additive it can act as a shredder and thus can contribute to the efficient particles size reduction [42,45]. On the other hand, materials with high values on Mohs hardness scale will not be affected equally as a soft powder by milling if they are a part of the same mixture, so one has to take this into account especially if analysis of particle size distribution is performed.

Particle size of starting powders plays an important role: desorption temperature of MgH_2 (one of the most promising materials for solid-state hydrogen storage) and reduced desorption temperature after milling of MgH_2 is determined by

particle size of commercial powder. In table 3, manufacturers, particle size, and desorption temperatures obtained by Differential Scanning Calorimetry (DSC) technique of some of the most commonly used MgH_2 powders are listed.

Comparing different MgH_2 powders and data from Table 3, it is obvious that particle size plays a vital role in desorption of H_2 from commercial MgH_2: lower desorption temperatures were obtained for powders with particle size smaller than 100 μm. By looking at data obtained from milled samples, it is interesting to notice that lower desorption temperatures are characteristic for samples with lower purity, where we can assume that MgO is present. Since MgO plays role as a catalyst [50], those samples show lower desorption temperature than samples with lower particle size and higher purity. So, although particle size plays an important role, it is more important to include a suitable catalyst in a mixture in order to improve MgH_2 characteristics.
By adding a suitable additive in small concentration to MgH_2, the performance of milled mixture can be significantly altered in favor of fast hydrogen sorption, reduction of sorption temperature, and better cyclability. Metals, metal oxides and hydrides, non-oxide compounds, and even complex hydrides can be used as additives in the process of milling [44,50--59,]. Some excellent results for hydrogen desorption were obtained when MgH_2 was combined with a small amount of oxides of transition metals (results listed in Table 4).

Table 4. List of commercial MgH_2 samples milled with different additives, and their desorption temperatures obtained by DSC method. Multiple temperatures correspond to multiple DSC peaks.

Ref.	**Com. MgH_2** Manufacturer, purity	**Milled MgH_2** DSC T_{des} (°C) /**rate** (°C/min)	**MgH_2 + oxide additive** DSC T_{des} (°C) /**rate** (°C/min)
[48]	*Alfa Aesar*, 98%	380, 466 / **5**	**1mol% Cr_2O_3** 410 / **5** 1mol% Nb_2O_5 415 / **5**
[49]	*Gold Schmidt AG*, 95%	323, 354 / **5**	**17mas.% Nb_2O_5** 264 / **5**
[50]	*ABCR Germany*, 98%	368 / **5** 381 / **10** 397 / **20**	**Cr_2O_3,** 338/**5**;359/**10**;379/**20** **TiO_2,** 328/**5**;348/**10**;372/**20** **Fe_2O_3,** 359/**5**;380/**10**;392/**20** **Fe_3O_4,** 360/**5**;379/**10**;396/**20** **In_2O_3,** 357/**5**;370/**10**;390/**20** **ZnO** 371/**5**;388/**10**;401/**20**
[51]	*Gold Schmidt AG*, 95%	336 / **5**	**10wt.% MgO** 262 / **5**
[52]	*Alfa Aesar, 98%*	450 / **10**	**20wt% A-TiO_2** 298,412 and 456 / **10** **10wt% R-TiO_2** 299,380 and 456 / **10**
[53]	*Alfa Aesar, 98%*	454 / **10**	**5wt% VO_2(B)** 350, 340 and 330 / **10**

DSC results listed in Table 4 show reduced desorption temperatures of hydrogen desorbed from MgH_2 in presence of small amount of transition metal oxides. Addition of Cr_2O_3 and Nb_2O_5 has reduced by 100 °C desorption temperature, measured at rate of 5 °C/min and followed by reduction of activation energy from 206 kJ/mol to 185 kJ/mol [48]. Authors explained this effect through formation of intermediate compound of $MgNb_2O_{3.67}$ during the desorption process. Excellent reduction of T_{des} (150 °C) was achieved with the addition of Nb_2O_5 but with very long milling time (200 h) [49]. Same desorption temperature reduction (152 °C) was obtained with the addition of MgO, where the mixture was milled for 100 h [51][54]. Authors concluded that higher oxide's metal electronegativity leads to the lower hydrogen desorption temperature [50]. Different kind of effects on hydrogen desorption were observed in mixtures of MgH_2 with oxides of titanium, iron, vanadium, zirconium, chromium and other TM´s, where besides reduction of T_{des}, kinetics of desorption was changed as well [50][52][53]. In those systems, hydrogen desorption occurs at three temperatures which is the result of the interfaces between high valence and low valence TM compounds. Those compounds are favoring electron transfer between Mg^{2+} and H^- at the interface which results in three-step desorption mechanism [55]. Another important observation was concluded in a case of MgH_2-VO_2(b) mixture: during cycling vanadium attacks hydrogen and partially changes from oxide to hydride phase [53] which was detected in the mixture after six cycles by XRD, and confirmed by Raman and FTIR spectroscopy. In this case, phrase catalyst is not exactly the best choice. Cycling showed a very fast desorption and absorption with full hydrogen capacity while DSC results showed reduction of desorption temperature of about 50 °C [53]. Since the first cycle act as a "working-out" cycle during which system goes through the process of stabilization and leveling unstable phase and defects, it is very important to run system on cycling in order to reach full understanding of each individual system.
Activation energies obtained using non-oxide additives, such as FeF_3,TiB, SiC, Mn, Fe, Ni, are listed in Table 5. [41][43][56-60]

Table 5. Activation energies for desorption of MgH_2 with non-oxide additives.

Ref.	Composite	Activation energy of desorption (kJ/molH_2)
[43]	TiB 5 wt%	173
	TiB-SiC 4.5-0.5 wt%	318
	TiB-SiC 0.5-4.5 wt%	289
[57]	MgH –Ti	71.1
	MgH –V	62.3
	MgH –Mn	104.6
	MgH –Fe	67.6
	MgH –Ni	88.1
[59]	NiS	75.34
[60]	TiH_2	77.4

Comparing oxide and non-oxide additives, it is possible to conclude in general that non-oxide additives shift low-temperature peak to lower temperatures and those peaks are usually very broad, while oxide additives have an influence on high-temperature desorption. This can be seen in Figure 6 where TPD results of MgH_2 with different additives are shown.

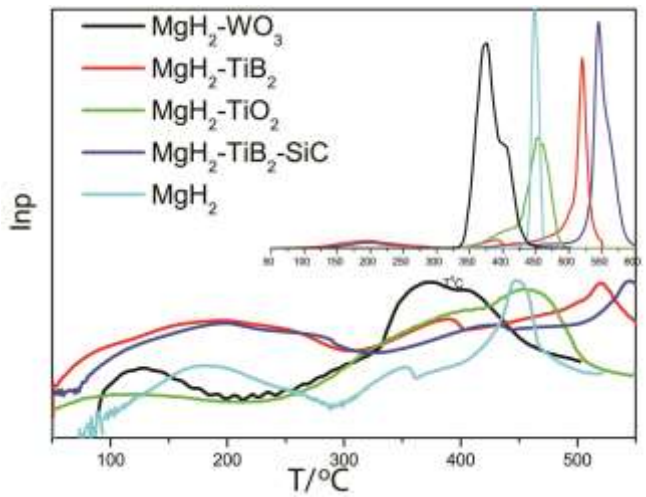

Figure 6. TPD curves of mixtures of MgH_2 and various oxide and non-oxide ceramics.

2.3 Severe Plastic Deformation tailoring the microstructure of Mg-alloys

Among mandatory conditions needed to deliver high hydrogen sorption kinetics in Mg-based compounds, are: a) creation of fine enough microstructures - particles and crystallites, b) implementation of high density of defects (glide planes, twins, high angle boundaries...). According to these requirements, for years Energetic Ball Milling (BM) was demonstrated as being very effective. Moreover, if adding specific additives to the primary MgH_2, fine and highly reactive powders are formed. More recently, other techniques, such as Severe Plastic Deformation (SPD) processes, have been proposed to fulfil here above conditions a) and b). Furthermore, most of these metallurgy processes definitively operate on bulk metal samples delivering interestingly textured materials, c) an interesting characteristic which is absent in BM MgH_2 powders. Additionally, BM is not so easy to upscale for mass production, being time, energy and man-power consuming; moreover, delivering highly pyrophoric powders. This is why progresses are expected by using SPD techniques e.g. Cold Rolling, Equal Channel Angular Pressing (ECAP), High Pressure Torsion, Fast Forging (FF)… as described in a generic reference [61]. Some advanced results are presented in [62-65]. Here, two SPD techniques are considered, since among the most promising in terms of up-scalability for safe and mass production, 1) ECAP applied to AZ31, a commercial type Mg-alloy, and 2) FF applied to Mg-Ni precursors. For the 1st case, no specific additive is used, so the analysis is mostly addressed to metallurgic state of processed materials before hydrogen cycling. For the second case, the contribution of Ni is questioned as forming the binary Mg_2Ni; well known to easy react with hydrogen.

2.3.1 ECAP to build reactive microstructures

Figure 7 shows the die environment of the ECAP machine which can be temperature monitored up to ~ 400 °C.

Figure 7. Up and right: the ECAP die used for SPD treatments applied to Mg alloys. The die setting on the press (down) is pushed towards the punch, which pushes the sample for channeling. Up and left: the open channeling die; down-left: tools forming different angle channels (L_E = 95°, 105°, 115°, 125° and 135°); right: ECAP system (die and punch)

We have systematically used ECAP to refine the microstructure of bulk AZ31 pieces (50x10x10 mm), for strain development and particle and crystallite sizes refinement. The level of strains developed in the billet due to the Severe Plastic Deformation process was anticipated by using a grid numerical analysis method and besides micro-hardness measurements performed all along the samples faces have allowed experimental controls. The ECAP treatments were operated under several experimental conditions, applying passes mode-A for which the square section sample is successively passed without any rotation reference to the channel geometry, and passes mode-B_C mode pass where a 90° rotation is applied from one pass to the next one. Comprehensive pictures can be found in references [66,67]. The critical experimental parameters that were questioned in terms of refinement of the microstructure are: 1) the mode of pass being A or B_C, 2) the number N_P of successive passes applied to the billet, the temperature T_P of dying, reference to the fragile/ductile behavior (T_{FD}) of the alloy and the dynamical recrystallization temperature T_{DC}. For so doing, the ECAP treatments were mostly operated at 175 °C and 275 °C. Using the numerical analysis grid method [68] the density of strains was established in all cases. It appeared that the most effective channeling route in terms of fast distribution of homogeneous and highest density of strains was the B_C mode as shown on figure 8.
This is confirmed by optical metallography and SEM analyses vs. the number of B_C passes (not shown here) with quite similar results as those received vs. temperature as shown in Figure 9.

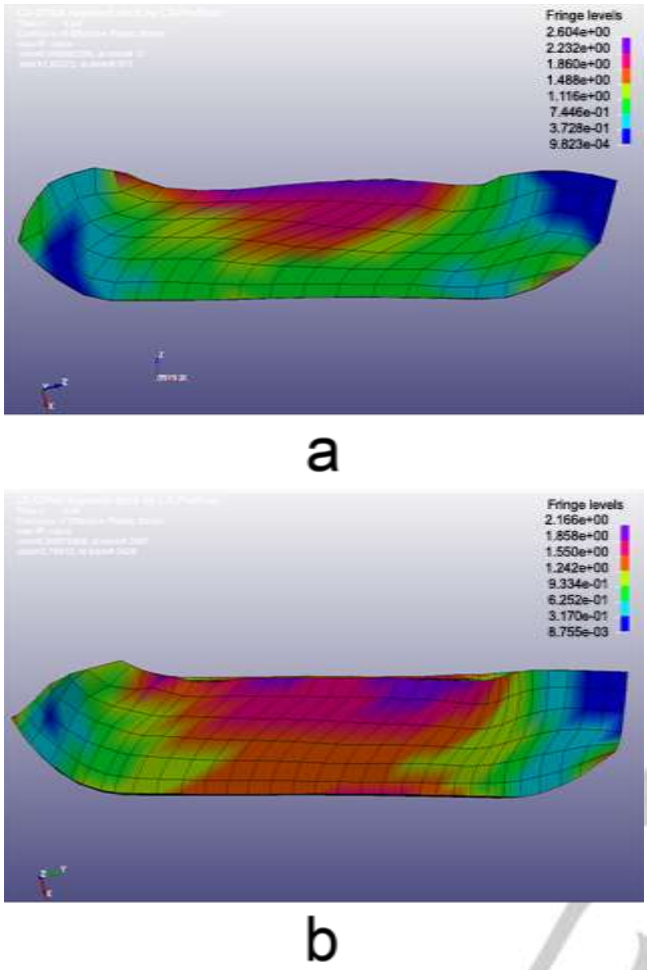

Figure 8. Strain intensity distribution after a 2nd ECAP pass: a- mode A, b- mode B_C.

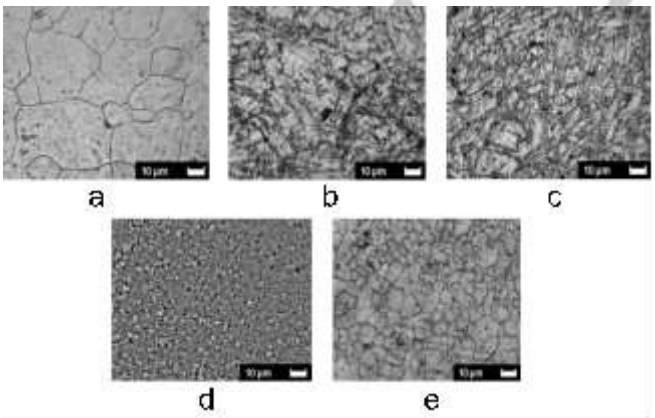

Figure 9. Grain microstructure versus temperature of AZ31 billets after 2 B_C passes: a - as received, b - 150 °C,c - 200 °C, d - 250 °C, e - 300 °C. Scale is 10 μm (lower left corner) for all images.

Parallel, we observe that the refinement of the microstructure operates similarly when 1) increasing the number of passes down to the fragile-ductile transformation temperature T_{FD} , 2) for only 2 passes if temperature is setting apart T_{FD}. Note if operating at high temperature a dynamical crystallization process can take place around T_{DC}, accounting for an additional heating when mechanically SPD deform the sample [68]. It is worth to note that after 3 passes, a minimum grain size of ~ 4 μm was achieved and then stabilized further, as shown in Figure 10.

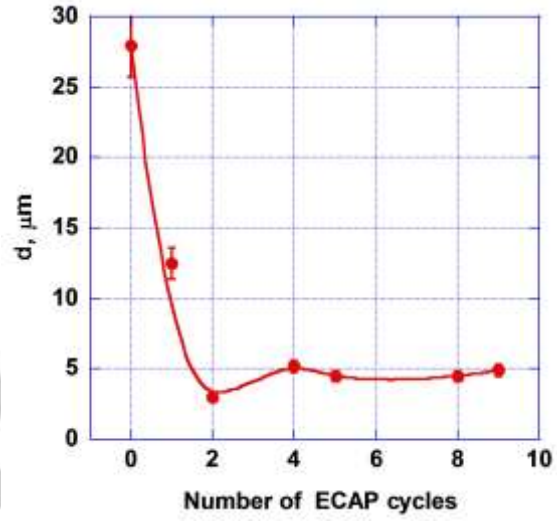

Figure 10. Impact of the number of ECAP passes on the grain size in AZ31 billet when ECAP treated mode B_C at ~ 200 °C. Note that after 3 passes, a minimum grain size of ~ 3 μm was achieved and then stabilized further.

Then the mean crystallite size and the mean density of stresses were determined from XDR patterns by refining the profile of diffraction lines angle by using the Williamson-Hall method [69]. Figure 11 shows the result for the B_C mode processed material for 9 passes at 250 °C. It is seen that the crystallite size is homogeneously of 300 nm without no strain density. As shown, an additional pass operated at room temperature (fragile regime) induces a smaller mean crystallite size, while the density of strains is markedly increased, with distribution effects depending on the crystal directions. For billets treated along mode A, very similar results as the latter ones are received. It means that the mode A operates “anisotropically” conversely to mode B_C (where a rotation of sample is operated in between passes), probably inducing less twins but a high dislocation densities. After 9 passes mode-A, the sample exhibits a mean grain size of ~ 125 nm but a 4 times larger strain density (even 10 times after a final RT process).

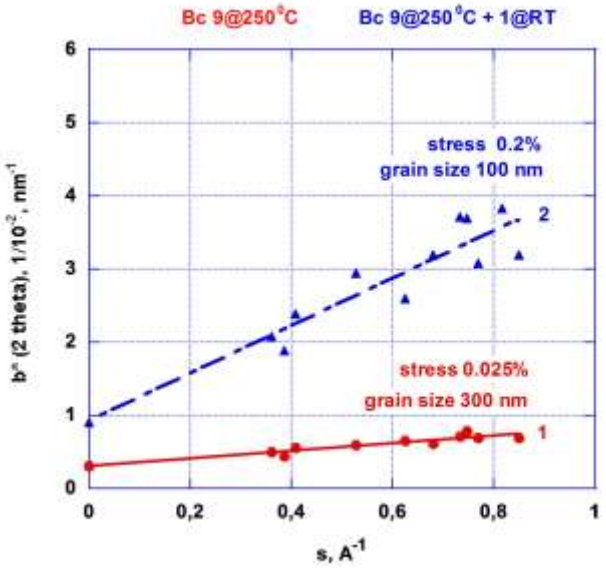

Figure 11. Williamson-Hall [69] plots allowing determine the crystallite size and the level of stresses leading modulate the linewidth of XDR patterns versus the Bragg angle (scattering vector s) for ECAP-treated AZ31 billets at 250 °C for 9 passes B_C mode (red) + 1 additional pass at RT (blue).

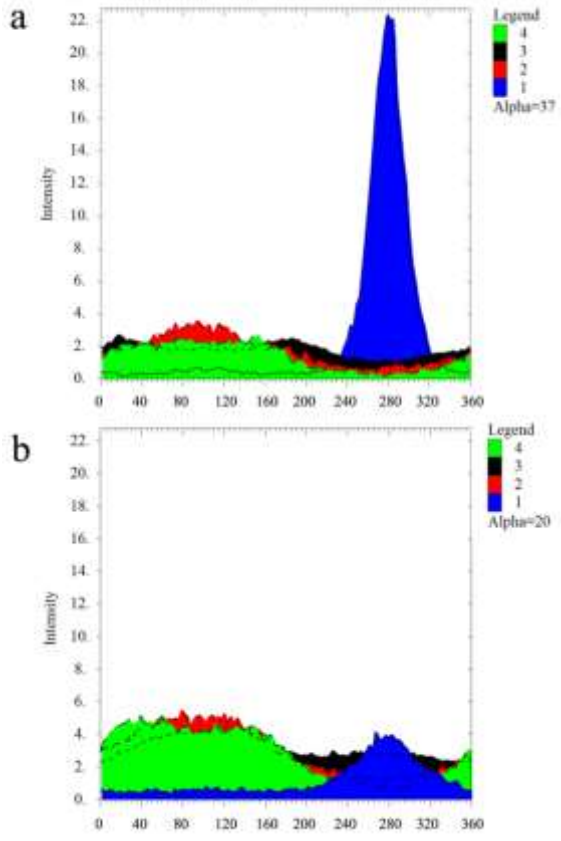

Figure 12. Integrated and normalized texture intensities for four main crystal planes **a** - mode A, **b** - mode B_C. Colors are for lines (hkl): blue (002), red (100), black (101) and green (110).

Small Angle Neutron Scattering experiments performed on 1 to 4 ECAP mode B_C at RT. Even for the 1 pass treated sample (~ mode A), SANS reveals ellipsoidal shapes which dimensions are comprised between 100 and 300 nm and 4-8 nm of intergrain boundaries, fairly agreeing with microscopy analyses.

It is worth understanding that the ECAP process also impacts the texture organization of the grains in the material. Quite different results are received depending on the processing modes A or B_C. Effectively many texture stereographic projections established from XRD diffraction, evidence the isotropic/anisotropic character of deformation along B_C/A. Very clear-cut pictures enlightening this aspect are shown in figure 12 where after integration along the stereographic axis, the normalized intensities of A and B_C textures are represented. Obviously the (002) plane orientation is merely developed for mode A, conversely to the "isotropic" picture found for mode B_C.

2.3.2 Hydrogenation kinetics and H-uptake of ECAPed AZ31 samples

Hydrogenation kinetics measurements were recorded on all the SPD processed AZ31 samples using a Hera PCI system after a short time powdering the fragile ingots was operated using a SPEX miller [70,71]. The applied conditions were 2 MPa at absorption and 15 kPa at desorption working at 350 °C. Interestingly, a general result was received allowing compare effects along mode A and B_C respectively whatever the number and temperature of passes are. Systematically the A processed sample kinetic traces reveal an initial incubation time for up to ~ 1 hour, a phenomenon never affecting the B_C mode processed samples. Two other characteristics have to be underlined. After 15 h recording time, the max- hydrogen uptake of 7.6 wt% was almost reached for all samples processed via mode B_C, the best being effectively the most ECAPed at the highest temperature (275 °C). Conversely H-uptake appears less effective for all the A-processed samples. Moreover, as was already underlined from numerical simulation, the mode B_C appears more effective ready in term of strains implementation than samples mode A. We anticipate that the different established textures could play significant roles on both the hydrogen diffusion and hydrogenation process. Figure 13 shows typical examples of hydrogen absorption kinetic traces for differently processed samples. It can be seen that even processed at 275 °C, the 3 passes mode-A sample absorbs less effectively hydrogen than the 8 passes mode-A one. Conversely the 175 °C and the 275 °C for 3 passes mode-B_C samples exhibits very similar absoption kinetics, both the profiles being much faster than the A-processed one. In fact an additionnal – but limited - gain in kinetics is observed when the B_C-sample is processed at 275 °C. For these last samples, almost a complete hydrogen saturation (~7.4 wt%) is reached after 15 hours of treatment. A 2nd absorption cycle was systematically applied to all samples in the same (P,T) conditions. Then it is important to mention that no incubation process (no delay) is noticed for the A-processed samples. Besides, if the initial kinetic is improved for all samples (A and B_C types), the 2nd saturation levels are observed less by

5-8% comparison made with the 1st cycle. From both observations, it can be anticipated that the microstructure has been somewhat modified during the (long) exposure at 350 °C in the titration set-up. It can be underlined that such a weak reduction of uptake was already observed, but plain performances were restored after implementation of a few H/D cycles [72], since the microstructure was again optimized.

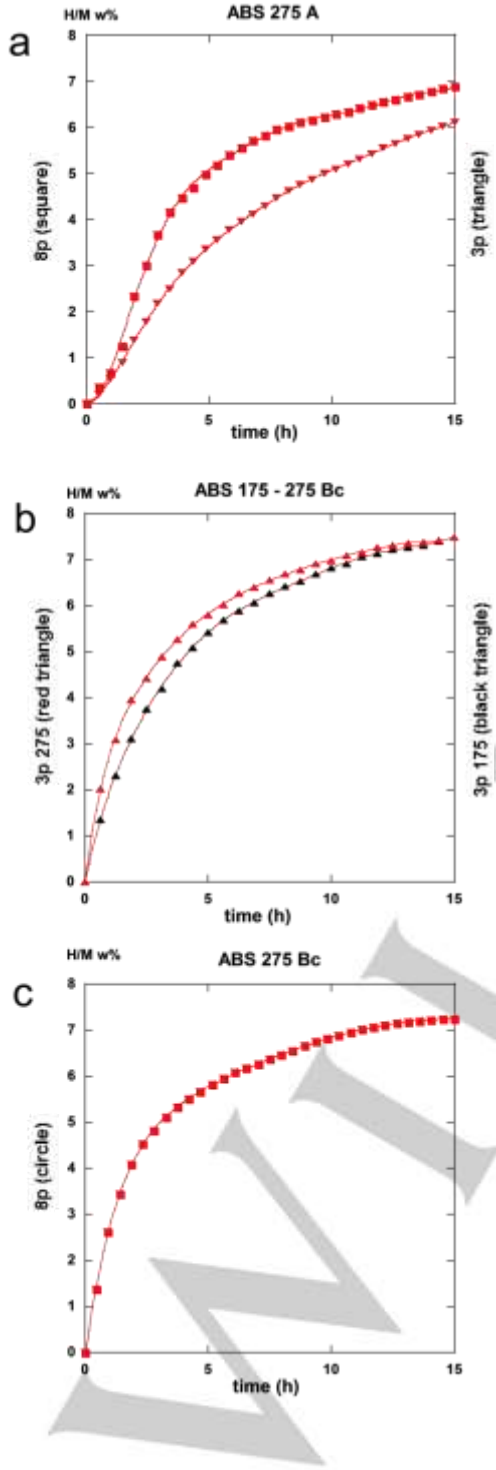

Figure 13. a: hydrogen absorption rate (H/M wt%) versus time as after ECAP process at 275 °C (triangle) for 3 passes (triangles) and for 8 passes (squares), respectively; b: Hydrogen absorption rate (H/M wt%) for B_C ECAP-treated billets: 3 passes at 175 °C (black) and 3 passes at 275 °C (red); c: for a sample processed 8 passes at 275 °C (red).

After the 1st absorption process, the samples were submitted to desorption. All samples react rather fast with a 90% hydrogen release in 30-50 min. Once more the best samples were those SPD-treated via the B_C mode and the faster at absorption the faster at desorption. A selection of desorption traces are presented in Figure 14, corresponding to the 2nd cycle. It can be seen that 90% to 95% of the absorbed hydrogen is then desorbed within 30 min.

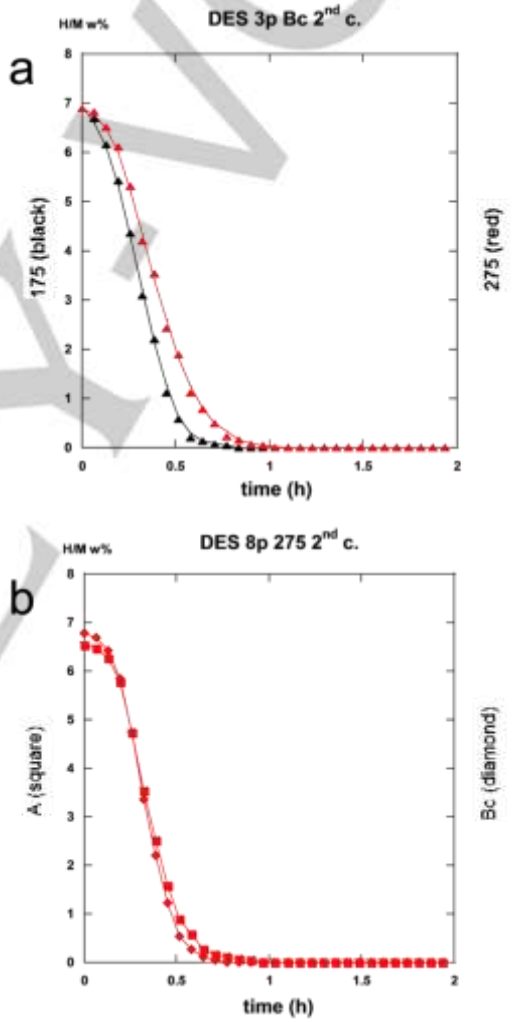

Figure 14. Comparison of the 2nd desorption rate traces (H/M wt%) of :a - 3 passes mode-B_C route ECAP treated at 175 °C and at 275 °C; b - 8 passes ECAP-treated at 275 °C for comparison of A and B_C routes

The 3p-B_C mode presents a more effective desorption rate when being processed at the lowest temperature (175 °C) than at the highest one (275 °C) as shown in Figure 14a. Besides after 8 passes of ECAP treatment, both the A and B_C ECAPed samples

at the highest temperature (275 °C) lead to very similar behaviors as shown in Figure 14b.

2.3.3 Modelisation of sorption properties

Both the absorption and desorption traces were tentatively modeled thus using either Jander, Johnson-Avrami-Melh-Kolmogorov (JAMK), Gistling-Broushtein or other kinetic laws [73]. No unique model can be retained as well fitting for both the absorption and desorption processes. Contrarily to homogeneous long time BM powders, it is obvious that the rapid mechanical treatments applied here – even if severe – have not installed a so homogeneous density of strains, defects and grain sizes distribution within large dimension samples. However, two regimes have been found suitable for the different absorption traces : 1) for the first period of hydrogenation all the traces agree well with a nucleation-growth model i.e. $(-\ln(1-\xi))^2 = kt$, and 2) for the approach to saturation an interface propagation at diffusion surface area can be considered for. In fact it is not possible to chose between the two progression laws $(1-(1-\xi)^{1/3})^2 = kt$ (constant diffusion surface) and $1-2/3\ \xi - (1-\xi)^{2/3} = kt$ (non-constant diffusion surface), probably because of some relative inhomogeneities in the particle sizes and shapes.

Lets consider both the filling value ξ_L where the propagation interface regime succeeds to the initial nuclation regime and the deformation factor DF defined as $N_P \times T_P$ (N_P the number and T_P the temperature of pass). Plotting ξ_L versus Log (DF) results in linear variations for both the 1st and 2nd cycle. These behaviors can be interpreted as follows for the 1st hydrogenation cycle:

1) The microstructure is made finer and finer and the density of strains is increased by an increasing number of passes, a similar result is received when increasing more and more temperature as shown in Figure 15,

2) Similarly the size of crystallites decreases parallel,

3) According to ref. [74] relative to hcp Mg deformations, at lower temperature the deformation regime leads to a major formation of high dislocation densities, conversely a higher temperature, the deformation results in less and less creation of dislocations, benefit made to formation of twins.

Consequently, the density of nucleation centers is made more and more important when the deformation factor (DF) increases. Therefore, the Johnson-Mehl-Avrami-Kolmogorov (JMAK) model becomes the predominating one and thus ξ_L increases accordingly. As a matter of fact, the B_C mode is the most effective immediately after a limited number of passes. Besides as seen in Figure 15 for long number of ECAP treatment both the respective variations of ξ_L converge to the same value (less and less difference in the A and B_C processing route). So, it can be anticipated that at 275 °C, both ECAP treatments will be made equivalent and a fully JMAK mode (nucleation-propagation) will be definitively installed to provide about 14 passes that are applied to the sample. For the 2nd hydrogenation cycle, the variation of ξ_L versus log(DF) appears as a reversed reference to the 1st hydrogenation one but, exhibiting a less marked variation. This reversed behavior is not surprising since during the rest time for hours at 350 °C, a dynamic recrystallization can take place, and the subsequent grain growth will be made at the expense of the smallest particles and the corresponding nucleation centers. So, for a part the JMAK process of absorption kinetic is found partly substituted by a Jander's type process of interface propagation.

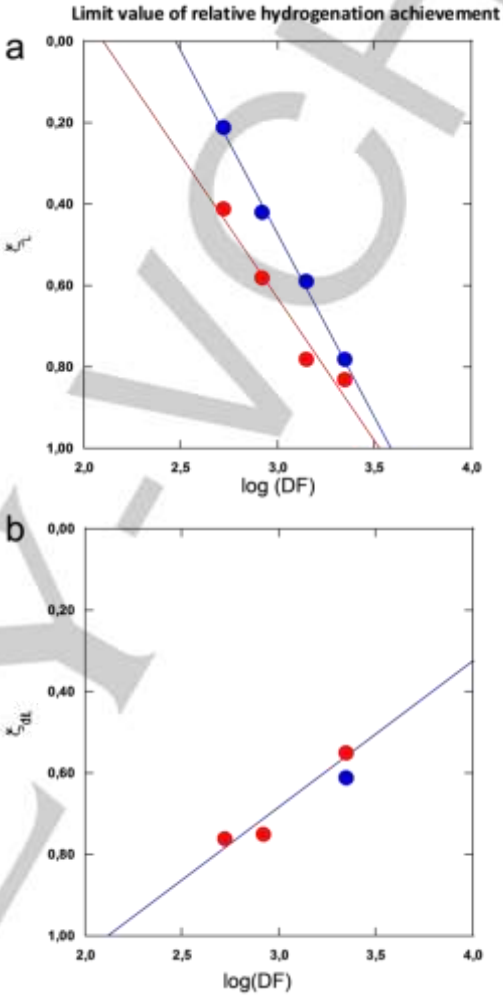

Figure 15. Limit value ξ_L of change in kinetic the mode vs log(DF). Blue dots are for ECAP mode A, red dots are for ECAP mode B_C, a: 1st hydrogenation cycle b: 2nd hydrogenation cycle (few experimental data)

2.3.4 Discussion on Mg-MgH_2 ECAP process

Conditions for easing hydrogen uptake in bulk Mg and its alloys such as AZ31 have been realized by using a Severe Plastic Deformation technique. ECAP can be successively applied to bulk materials for mass and rapid production. In the present study, the refinement of grain and crystallite sizes, the realization of high density of defects, the formation of texture are found as the key parameters that allow good hydrogenation/dehydrogenation kinetics. For the first time, a microscopic mechanism allowing a better understanding of the absorption kinetics is proposed. If effectively measured kinetics remain rather low in comparison to those obtained by Ball Milling MgH_2 powders with specific additives, this apparent lack of

performance is not so detrimental for mass storage application of MgH_2. In fact, the driving parameter for the optimum management of a medium to large scale of MgH_2 based tank is not the sorption kinetics but the heat management of the exothermic/ endothermic processes [75,76]. So, too fast reacting materials can make operating the system more difficult. Besides the maximum hydrogen uptake of 7.6 wt% was almost reached, comparison made with the non-ECAP-treated AZ31 (~0.5 wt% for 15 h absorption and for 2 h desorption). However, a good compromise can be expected with introduction in the based alloy, of some amount of additives that could be inserted by SPD as effective interfaces, e.g. in the grain boundaries.

2.3.5 Fast forging of Mg-Ni powders

Fast Forging is operated at a lab scale by using the forge pictured in Figure 16a on a cylindrical sample. The hammer of mass 150 kg, falls from ~1.5 m on a piston in direct contact with the sample setting on an anvil disposed in a specially designed chamber as shown on Figure 16b. In the chamber, evacuated then filled with 5N purity Ar gas, the sample can be easily heated by means of a high frequency coil, the temperature being measured using a two wave-lengths optical pyrometer. The Mg-based sample - 13 mm diameter x 20 mm height - is forged at the rate of 5 x 10^{-3} sec., typically resulting in a flat disk - ~ 30-35 mm diameter x 2 mm thickness -. In order to avoid a burst effect of matter at shock, which could result in less mechanical energy transmitted to the sample, the latter is inserted in a thin wall Cu or Fe sheath as illustrated in Figure 17. The starting samples here considered were mixtures of powders: Mg (40-100 µm, 98.5% purity from McPhy) and Ni (30-40 µm, 99.5% purity from Neyco. Different compositions were prepared with 14, 22 and 50 wt% Ni… first actively mixed, then compacted in a die using a 1 T/cm^2 press and finally inserted in metal sheaths, as shown in Figure 17 a,b,c. From forging experiences, the Fe cylinders were preferred to the Cu ones, allowing a better compactness, since less ductile than Cu, additionally when heated with the sample.

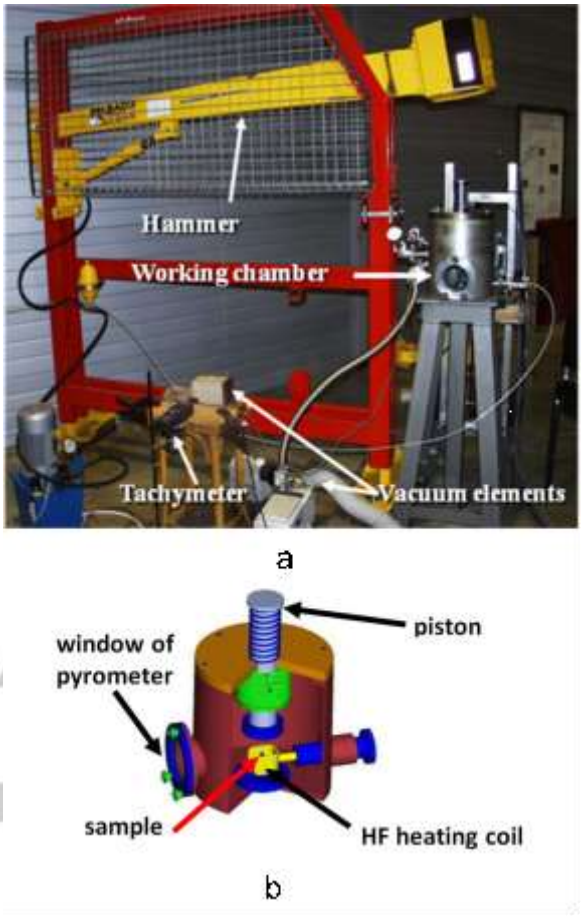

Figure 16: Fast Forging instrument with a - the hammer, the chamber and ancillaries, b –details on the chamber with the piston, HF heating coil for the sample, window for pyrometer temperature measurement. The chamber is maintained under high purity Ar atmosphere during forging (see down)

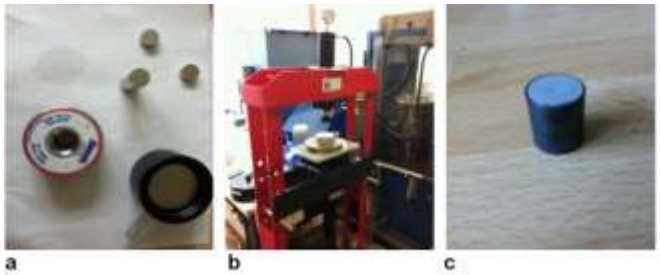

Figure 17: Preparation of the Mg-Ni sample, a – dying the mixture of powders, b – pressing pellets up to 1 T/cm^2, 3 – a cylinder pellet is inserted in Φ 13 mm diameter sheath (Cu or Fe).

A very important parameter to be considered during the SPD process by Fast Forging is the effective temperature of the sample at shock; a noticeable part of the kinetic energy is transformed to heat. An estimate of the increase of temperature was computed [77], indicating at least 100 °C more than that maintained due to the external heating. Another aspect difficult to account for is the instantaneous dissipation rate of heat in the large masses of both the piston (hammer) and the anvil. This is

why most experiences were made heating the sample a various temperatures, from RT to less than 500 °C.

2.3.6 Fast Forging as a fast alloying technique

As a general result, the fast forging process based on the initial 14 and 22 wt% Ni was received as a mixture of 4 phases: the hcp Mg, an alloy which composition is related to the eutectic one, the Mg_2Ni compound and the fcc Ni. Determining factors are the proportions in the initial mixture but the temperature of forging directly monitors the reaction and the final repartition of the phases. For example, a 22 wt%-Ni sample fast forged at ~ 480 °C reveals presence of the 4 phases; however, with a few amount of metal Ni only, as shown on Figure 18. From XRD analysis hcp Mg is seen with a marked texture favoring the (002) line. Conversely the hexagonal compound Mg_2Ni (space group *P6$_2$22* a = 0.5216 nm, c = 1.320 nm) which was developed in-situ during the forging exhibits insignificant texture and only a few amount of Ni remains can be identified by the weak (111) line.

Depending on the temperature applied to the sample at fast forging, the proportions of the different phase are modified and higher the temperature is lower in the pure Ni content, even being absent due to its total conversion in Mg_2Ni. Typically the fast forged binary "22 wt% Ni" materials could be composed of ~ 69% of Mg and ~ 31% of Mg_2Ni when operating at temperatures lower enough to prevent any melting of one or both the received compounds (508 °C for the Mg-Ni eutectic and 650 °C for Mg).

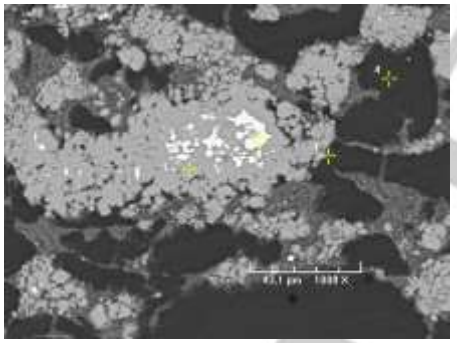

Figure 18: SEM picture of a 22 wt%-Ni sample fast forged at ~ 480 °C revealing presence of the 4 phases – black is ~ Mg, grey dark is ~eutectic composition, light grey ~ Mg_2Ni and white is ~ Ni.

2.3.7 Hydrogenation of Fast Forged Mg-Ni composites

Hydrogenation of the fast-forged compounds was operated using a Hera PCI. Here are presented some aspects of the kinetic process. The hydrogenation at 325 °C under 2 MPa H_2, of the 14 wt%-Ni and 22 wt%-Ni containing materials as forged at about 480 °C, were operated first. Since numbers of H/D cycles must be applied to improve the H-uptake of both samples, it appears that the former absorbs ~1.9 and the latter ~3.1 wt% H at the 10th cycle after ~1/2 h rest time. Figure 19a shows the progression of both the uptakes for the two samples. Obviously both performances remain far from the maximum uptake (~6.8 and 6.3 wt% respectively). However, it is worth to note that the less Ni doped material exhibit the weakest acceleration in terms of kinetic improvement with the number of cycles, notwithstanding a larger theoretical H_{max}. This may agree with a conclusion of ref. [78] for which after ECAP, Ni-supersaturated and deviation from stoichiometry in small Mg_2Ni grains can lead to chemical in-homogeneities improving hydrogen storage. However, please note that the here used FF technique induces the formation of Mg_2Ni from Mg and Ni grains in one shoot, but conversely HEBM, HPT and ECAP are accumulative techniques of different type defect density and reduction of the grain size as demonstrated in Part II and experimented in refs. [79-82].

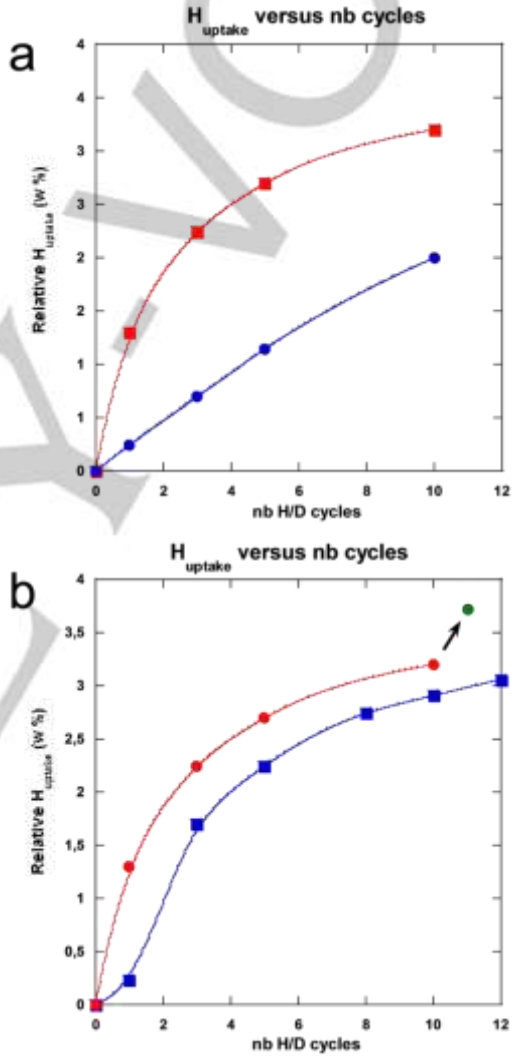

Figure 19. Amount of absorbed hydrogen (in wt%) versus the number of hydrogenation cycles at 325 °C under 2 MPa H_2 a - for Mg/Mg_2Ni composites fast forged at about 480 °C with: blue - 14 and red - 22 wt% Ni, b - for Mg/Mg_2Ni composites (22 wt% Ni) fast forged at: red – 480 and blue ~400-450 °C. One more cycle operated at 345 °C the latter exhibit a net hydrogenation benefit (green dot)

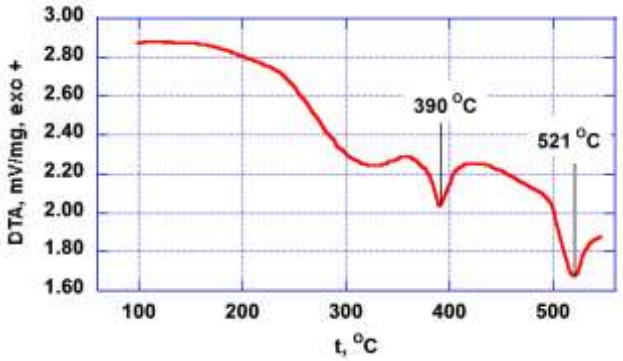

Figure 20. DTA analysis of a 22 wt% Ni fast forged at ~ 480 °C showing the $Mg_2NiH_4 \rightarrow Mg_2NiH_{0.3}$ transformation in the range 240 °C to 350 °C followed by the MgH_2 desorption starting at ~ 360°C. Additionally the eutectic melting was recorded at ~ 506 °C.

Figure 19b allows compare the H-uptake progression at 325 °C under 2 MPa H_2, of two 22 wt%-Ni containing materials, 1 - shown above as FF at ~480 °C, 2 – as FF at lower temperature (est. 400-450 °C) with more Ni remains. After 10 to 12 H/D cycles, the H_{uptake} remain close to 3.1-3.3 wt%. But the 2nd material is cycled one more but at a higher temperature of 345 °C and immediately the H_{uptake} is found larger close to 3.75 wt%.

This means that for this type of fast forged materials without any repetitive nano-structuration, the thermodynamic equilibrium between different non-hydrogenated and hydrogenated phases reveals obviously critical as shown on DTA traces on figure 20. In fact, between 240 °C and 350 °C, Mg_2NiH_4 transforms to the hydrogenated solid solution $Mg_2NiH_{0.3}$ [83,84], immediately after the desorption process of MgH_2 starts at 360 °C. Reversely, according to hydrogenation processes, synergic 3-active phase effects were proposed in [85-87] from in-situ experiments and mainly argued in a critical temperature range apart 350 °C [88].

To summarize, the Fast Forging technique was used to generate in one shoot interpenetrated $Mg/MgNi_2$ microstructures from initial mixtures of Mg and Ni powders. Indeed, both temperature and rate of forging are determining parameters leading control the metallurgical state of the as received material, i.e. the potential reactivity with hydrogen. Anyway, as for many other $MgNi_2$ based materials, the reaction with hydrogen was found rather slow and depending on several factors such as the initial Mg/Ni ratio, temperature of the sample, the H_2 gas pressure, the number of H/D cycles. As well, the formation of a corresponding mixture of MgH_2 and Mg_2NiH_4 is pressure and temperature dependent, where the solid solution $Mg_2NiH_{0.3}$ should actively take part in the hydrogen transfer. So, many parameters have to be adjusted and corresponding properties analysed to make performant and really up-scalable this original technique.

3. Theoretical approach to destabilization of hydrogen storage materials

3.1 Review of theoretical studies of MgH_2

A number of theoretical and computational investigations of MgH_2 and related systems have been reported.

Stander and Pacey [90] performed a Born–Mayer type of calculations of the MgH_2 lattice energy assuming that compound is purely ionic. The obtained energy value was larger than the experimental one and this discrepancy was interpreted as indication of a covalent bonding contribution to MgH_2.

Noritake *et al.* [91] confirmed that bonding in MgH_2 is a complex mixture of ionic and covalent contributions. Some additional information about MgH_2 was recently obtained using vibrational spectroscopy and ab initio calculations [36].

Ab initio calculations of Schimmel *et al.* [92] suggest that hydrogen diffuses through the Mg metal phase, jumping between octahedral and/or tetrahedral interstitials. They have also demonstrated that for large metallic particles and low temperatures, hydrogen diffusion through the Mg metal is not expected to be the limiting factor of H kinetics, unless hydrogen enters Mg matrix merely via small catalyst particles, lowering in that way the cross section of the H diffusion channels.

Some other Density functional theory (DFT) based calculations performed to study the formation and diffusion of H vacancies on MgH_2 surfaces and in the bulk [93] suggest that surface desorption is more likely the reaction rate limiting step than H diffusion. Consequently, finding an effective catalyst, which could facilitate H desorption from the MgH_2 surface, is crucial for improving its overall sorption performances.

The transition metals have been used as catalysts for hydrogen sorption, to support the breakup of molecular hydrogen into atoms and their moving into, or out of MgH_2 [41,57,94-100]. However, the observed catalytic mechanism is still not adequately explained. Despite numerous theoretical simulations taking into account the substitution of Mg in MgH_2 compound and MgH_2 clusters with transition metal (TM) atoms [101-105], a further improvement of the hydrogen kinetics requires a full knowledge of intrinsic mechanisms by which TM alloying affects the compound properties.

3.2 Methods used in theoretical research

The theoretical research presented provides a detailed insight into the mechanisms that determine different interactions in pure and doped metal-hydride systems – potential candidates for hydrogen storage in solid state. Systems based on magnesium hydride doped with the entire 3d TM series were studied [106,107]. Electronic properties of these systems were obtained using *linearized augmented plane wave* (LAPW) [100] *and projector augmented wave* (PAW) [101] methods for accurate and efficient solving of the DFT equations.

For the most of the calculations presented in this review the LAPW method has been used, as implemented in WIEN2k code [110]. The method is well known for its robustness and applicability on wide range of solid state systems. It is based on

unit cell partition to non-overlapping atomic muffin-tin spheres, where the fast oscillating wave functions are described with atomic-like functions, and interstitial space where the plane wave expansion is used. The linearization in energy is another simplification of the problem, with a small error being introduced as a price payed for a large speed-up of the method.

Abinit code [111] and Troullier-Martins pseudopotentials [112] were used for all calculations in the investigation of H vacancies mobility near the surface of MgH_2. The same code and its PAW implementation have been used for transition metal doped MgH_2 additional calculations.

Carr-Parinello method molecular dynamics has been performed as implemented in pseudopotential based CPMD code [113,114]. Special emphasis was placed on the examining properties of the charge density scalar field ρ(r) within a frame of Quantum Chemical Topology (QCT) methods [115].

The first method used is the Quantum Theory of Atoms in Molecules (QTAIM), as proposed by Richard Bader [116]. Its foundation lays on the topological analysis of the charge density - ρ(r), by which the space of a molecule or a crystal structure can be divided in a unique way into basins corresponding to atoms of investigated system. Scalar field of charge density and its gradient vector field contain, by definition [117], complete information about the ground state of a molecular or a crystal system, its bond properties, cohesion, and stability. The topological analysis comes down to solving so called the zero-flux surface equation and finding a set of points in which the charge density flux is equal to zero. In this way one gets the lowest of the valleys and the highest of the hills of the charge density, respectively one can obtain stationary (critical) points, a local maximum, minimum or saddle of ρ(r). These points correspond to the elements of structure and reveal the concept of atom, bond and structural stability.

The second method used in investigation of these systems is complementary to QTAIM and called the Non-Covalent Interaction (NCI) approach. This method also relies on investigating properties of ρ(r) throughout the quantity called *reduced density gradient* (RDG)

$$s = \frac{1}{2\left(3\pi^2\right)^{1/3}} \frac{|\nabla\rho|}{\rho^{4/3}} \quad (1)$$

and enables identification and visual representation of various electronic and electrostatic interactions in real space [118,119]. Meaning of RDG becomes much clearer by taking into account that this quantity has a profound importance in constructing *generalized gradient approximation* **(**GGA**)** functional in DFT and represents a measure of local deviation of ρ(r) relative to homogeneous electronic gas. A comparative analysis of s and ρ is then able to give insight into different interactions and to place them in the corresponding part of the real space: high s and low ρ define the "non-interacting" region, low s and high ρ the domain of covalent interaction and low values of both quantities identify "non-covalent" interaction region. By introducing a sign of the second eigenvalue of Hessian matrix - $sgn(\lambda_2)$ into analysis, one can also gain additional information about an interaction in the "non-covalent" region by presenting RDG as a function of $sgn(\lambda_2)\rho$ [120]. Negative values of λ_2 are indicative of bonding interactions since charge density is locally accumulated in that case.

3.3 Pure MgH_2

The beta MgH_2 crystalizes in tetragonal rutile type structure, with the symmetry of space group *$P4_2/mnm$* (No. 136) (see figure 21). There are total of 6 atoms per unit cell. Every Mg atom at *2a* (0,0,0) position is surrounded with 6 H atoms in the vertices of slightly distorted octahedron, with four coplanar atoms in basal plane and two (top and bottom) atoms at similar distances, while every hydrogen atom at *4f* (x,x,0) position is surrounded with three coplanar Mg atoms with nearly perfect 120° angle separation. Hydrogen sites possess additional internal degree of freedom. Experimental lattice parameters are a=b=0.4501 nm and c=0.301 nm, while the free fractional coordinate is x=0.304 [121], with Mg-H interatomic distance equals to 0.195 nm.

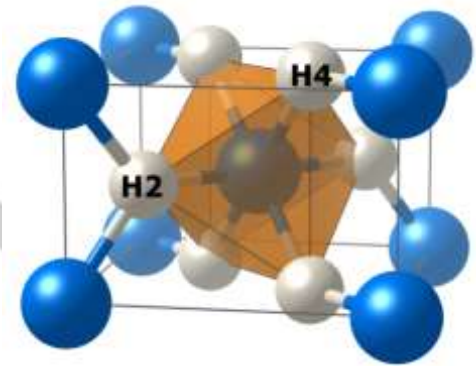

Figure 21. Unit cell of beta MgH_2. Mg – blue spheres, H – white spheres. First coordination octahedron is colored orange. H4 and H2 stands for four coplanar and two (top and bottom) H atoms in the first coordination octahedron.

Detailed electronic structure of MgH_2 obtained using LAPW with GGA exchange correlation potential as parametrized by Perdew, Burke and Ernzerhoff [122] is presented in Figure 23 [107]. Distinct feature of MgH_2 electronic structure is a broad energy gap (E_g) of 3.8 eV. There is, however, a discrepancy between experimentally obtained value of 5.16 eV [123] or 5.6 eV [124] and theoretical results, an issue generally attributed to the calculation method and to the choice of the exchange-correlation potential (GGA is known to underestimate E_g width and to some extent the valence band width. The valence band is composed mainly of strongly hybridized H-s and Mg-3p states, with two distinct peaks, the one positioned at -2 eV and the other just below the Fermi level. The origin of multiple peak structure is sometimes attributed to additional H-H interaction. The bottom of the valence band comprises of some Mg-s states as well, with a maximum at -4 eV. The conduction band (EC) bottom is predominantly of Mg-p, and to some extent of Mg-s origin.

The obvious way to analyze charge accumulation/depletion at atomic sites when using muffin-tin (MT) based methods is the

charge integration over MT spheres. The value of results obtained is often disputed due to the fact that MT radii are arbitrarily chosen (with some obvious constraints), but still they can serve as a rough description of processes taking place during formation of chemical bonding. In pseudopotential calculations of MgH_2, Yu *et al.* [123] determined ionic radii assuming that nearest neighbor (NN) ions are in immediate contact with each other and found values of 0.06 nm and 0.126 nm for Mg and H, respectively. The ionic charges calculated using MT radii are +2 for Mg and -0.6 for H, providing a picture of an almost purely ionic compound and the interstitial charge is 1.6 e/unit cell. Trends of the charge confined inside the Mg and H MT spheres, (+1.93 e for Mg, -0.34 e for H, with 3.85 e in the interstitial region) go toward results of [123] and known empirical relations between the ionic radii of Mg and H and their charge states [91].

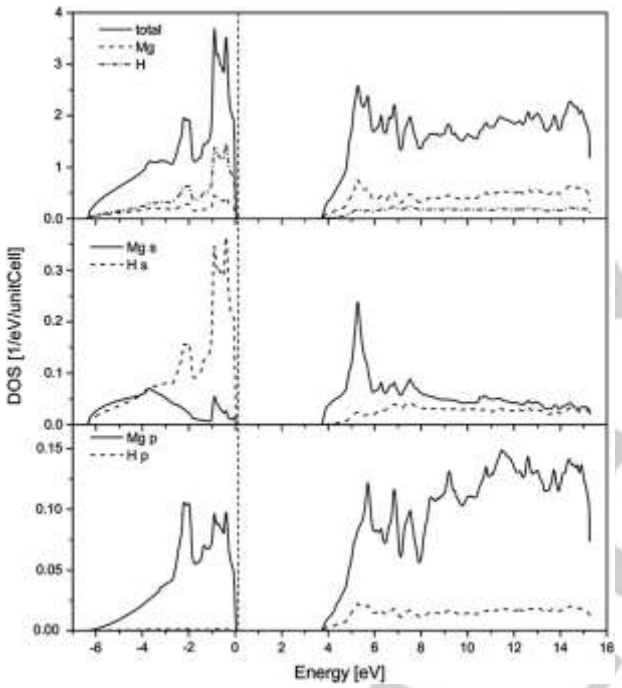

Figure 22. Detailed electronic structure of beta MgH_2. Reproduced with permission from N. Novaković, Lj. Matović, J. G. Novaković, I. Radisavljević, M. Manasijević, B. P. Mamula, N. Ivanović, Int. J. Hydrogen Energy 2010, 35(2), 598-608 [107].

It should be noted that calculations of the hypothetical compound consisting of H atoms alone, placed at same lattice positions as in original MgH_2 have provided energy bands with a narrower valence band and a significantly larger energy gap (around 5 eV). This is connected to the determined strong Mg-H hybridisation and the fact that bottom of the conduction band is predominantly of Mg- character.

Valence charge densities in (110) (above) and (001) (below) crystallographic planes are presented in Figure 23. Mg atoms are strongly charge depleted with ‘‘borrowed’’ charge not completely located at distinct H ions, but shared between the two neighbour H’s promoting a resonant bonding between them. This feature is visible also in the (001) plane. Such a charge distribution suggests that besides a dominant Mg-H ionic contribution, the H-H bonding contribution to the compound stability is not negligible.

In Figure 24 some of the results of QTAIM charge density analysis are given for MgH_2. Blue lines correspond to Mg-H bonding paths, while red one correspond to found H-H bonding path. Blue open circles correspond to bonding critical points (bCP), while green correspond to ring critical points (rCP). Non-intersecting red lines around atomic positions uniquely define zero flux surfaces of charge density gradient and “atoms” boundaries in the crystal lattice. As expected, there are six bCPs around each Mg and three coplanar bCPs around each H atom. Very important feature of the presented topology is the existence of the bCP between the closest H atoms in the basal plane of the MgH_2 unit cell, thus indicating the existence of H-H bonding in MgH_2. Although H-H bonding distance is quite long and this interaction is rather weak, it gives a non-negligible contribution to dominantly ionic cohesion of MgH_2 [123-126].

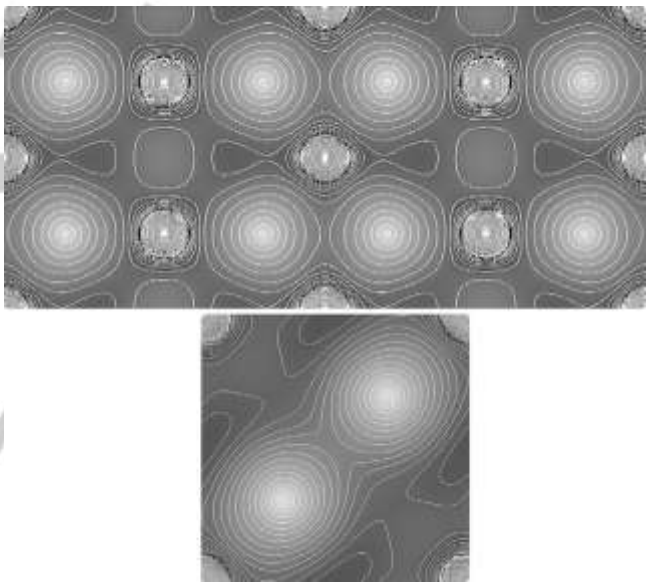

Figure 23. Charge densities of MgH_2 in [110] and [001] planes. Reproduced with permission from N. Novaković, Lj. Matović, J. G. Novaković, I. Radisavljević, M. Manasijević, B. P. Mamula, N. Ivanović, Int. J. Hydrogen Energy 2010, 35(2), 598-608 [107].

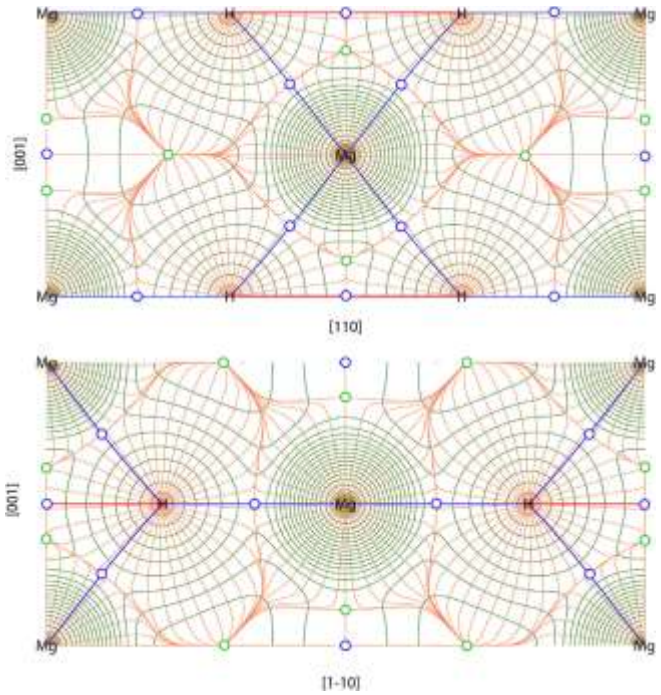

Figure 24. Charge density isolines (green), superposed to vector field lines of charge density gradient (red) in (110) and (1-10) crystallographic planes of MgH_2. Blue hollow circles are bonding critical points, green are ring critical points Reproduced with permission from B. P. Mamula, J. G. Novaković, I. Radisavljević, N. Ivanović, N. Novaković, Int. J. Hydrogen Energy 2014, 39(11), 5874-5887 [104]

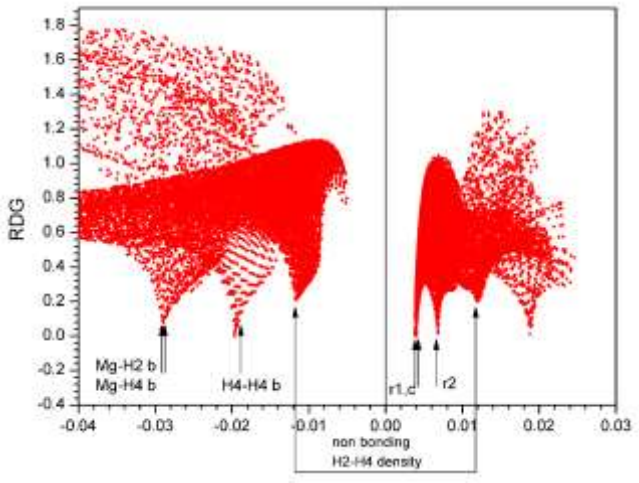

Figure 25. Reduced gradient density as a function of $sgn(\lambda_2)\rho$ in the first coordination polyhedron of Mg atom in pure MgH_2. Blue arrows indicate positions of characteristic details of ρ(r) compared to the results from topological analysis.

NCI plot for the first coordination polyhedron of Mg atom in MgH_2 is presented in Figure 25 along with indicated positions obtained from a topological approach.

On the left side of NCI plot, there are three minimum values of reduced density gradient s(ρ) indicative of bonding interactions. Along the direction between the nearest neighbours Mg-H2 and Mg-H4 there are bCP's that almost coincide in value and there is also interaction between second neigbours H4–H4. In this NCI plot there are also two peaks approximately with the same value (|ρ|~0.08) both on the negative and on the positive side of $sgn(\lambda_2)\rho$. According to the standard interpretation in this method, these peaks define non-interacting regions since they do not fulfill the zero gradient condition and thus are not critical points. Another way to display results presented in Figure 24 is to plot three-dimensional isosurface for chosen s(ρ) value, which allows an insight in spatial localization and distinction of bonding (blue) and non-bonding (red) interactions like in the two-dimension RDG plot. Values of s(ρ) in Figure 26 are chosen to emphasize details of interest. Blue disks match areas around bCP (Mg-H4) and blue-red areas along the direction between H4 atoms correspond to the rCP-bCP sequence. Non-interacting regions between H2 and H4 second neighbour atoms are tiny red-blue areas the most obvious for s=0.22 and are, in fact, symmetrical relative to (110) and (1-10) plane and are a part of redistribution of the charge that stabilizes the system.

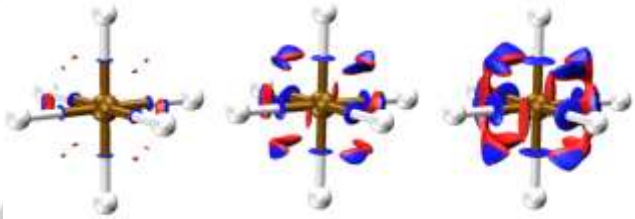

Figure 26. NCI isosurface in the first coordination polyhedron of Mg atom in MgH_2. Golden central sphere is Mg atom and white ones are H atoms. From left to right values of s(ρ) are 0.22, 0.3 and 0.4.

3.4 Vacant MgH_2 - surface and bulk mobility of H atoms and vacancies

Answering the question which of several desorption/absorption steps are responsible for slow kinetics has been the subject of numerous research papers. Comparison of the theoretical and experimental results led to the conclusion that the rate-controlling step of the MgH_2 dehydrogenation is surface recombination of hydrogen [127,128]. Du *et al.* have found that, among several candidates, (110) MgH_2 surface has the lowest energy barrier for the recombinative hydrogen desorption. They have performed NEB calculations and determined that barrier for the H-vacancy diffusion from the surface to the subsurface layers is around 0.7 eV, much smaller than the hydrogen desorption energy from the (110) MgH_2 surface (1.78-2.80 eV)

[93,129]. Investigation of the charged native point defects in MgH_2 and indicates that in absence of impurities and under extreme H-poor conditions, the lowest formation energies are for positively and negatively charged hydrogen vacancies. In extreme H-rich conditions, the lowest formation energies are for negatively charged magnesium vacancy and negatively charged interstitial hydrogen. The hydrogen-related vacancies are found to be highly mobile, with migration barriers between 0.10 and 0.63 eV, depending on the vacancy type [130].

However, little data exists about the dependence of the H desorption energy and the sub-surface vacancies formation energy on the number and distribution of surface H atoms. In this work we present the results of calculations of these dependences for the (110) MgH_2 surface, that provide all the details necessary to understand the H-desorption kinetics from MgH_2 at high concentration.

In our theoretical study of vertical and horizontal mobility of H vacancies, we have found that the observed trend of monotonic slow increase and saturation of vacancy formation energy at subsurface atomic layers further away from the surface is similar to the one observed in the literature [93,129]. The situation is completely different for lower surface H coverage (see figure 27), with the vacancy formation energy considerably lower in the 1st and especially in the 2nd layer (1.11 to 1.35 eV). The formation energy of H vacancy in the 6th layer is again similar to the (a) – zavisi da li je konkretno fully covered surface, as expected, due to surface effects being "screened" by many atomic layers in between. The influence of surface coverage on surface barrier profile emphasizes the importance of rate of hydrogen recombination at surface in order to keep the surface as "hydrogen-free" as possible [132].

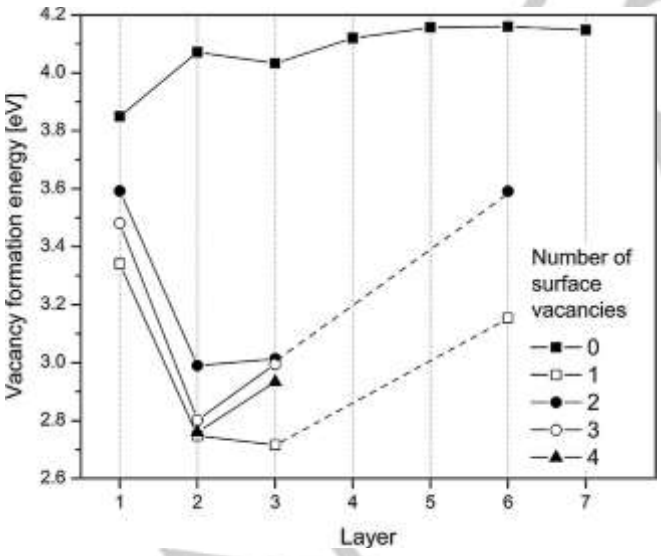

Figure 27. Neutral H- vacancy formation energies as a function of surface H coverage. Reproduced with permission from S. Kurko, I. Milanović, J. Grbović Novaković, N. Ivanović, N. Novaković, Int. J. Hydrogen Energy 2014, 39(2), 862-867 [131]

Influence of surface coverage on subsurface hydrogen vacancies is investigated thoroughly down to third atomic layer (Figure 28). It has been found that the lowest H vacancy formation energy is obtained for only one surface vacancy present (25% surface coverage in the model). The results also suggest that the most mobile are the vacancies in the vicinity, or immediately under the surface vacancy.

These results suggest that maintaining the optimal surface concentration of H atoms during the H-desorption process is crucial for the improvement of H desorption kinetics. This could be done, for instance, by incorporation of suitable impurities, or defects, at the (110) MgH_2 surface and in the immediate subsurface layers, which would facilitate the initial stages of the H-desorption process (surface vacancies creation) and control the subsequent H-diffusion from the bulk toward the surface.

During hydrogen desorption from MgH_2 thin films [38], a change in the colour and brightness of the samples was observed, before the metallic phase was formed. We have performed calculations of the optical properties of bulk MgH_2 with different concentrations and different possible charge state of H-vacancies (figure29).

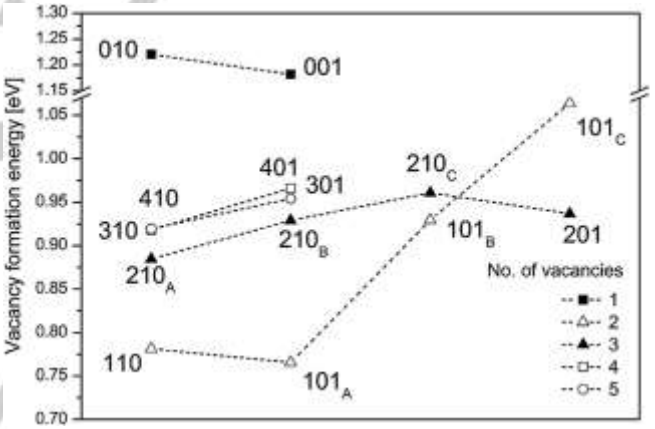

Figure 28. Horizontal neutral H vacancies mobility expressed using vacancy formation energies of different surface and subsurface configurations. Position on th ex axis correspond to configurations with vacancies further away from surface Reproduced with permission from S. Kurko, I. Milanović, J. Grbović Novaković, N. Ivanović, N. Novaković, Int. J. Hydrogen Energy 2014, 39(2), 862-867 [131]

The results show that even at modest H concentration (~3.125 at% in this model) visible region of spectra is influenced considerably. The widening of vacancies states due to vacancies concentration increase during desorption process will have more profound effect on adsorption of MgH_2. This means that changes in colour, brightness, and the partial loss of transparency of the samples can in principle be explained by the appearance, position, structure, and width of the H-vacancy band within the electronic structure energy gap. The proposed explanation also supports previous experimental findings concerning the influence of substoichiometric hydride phases on MgH_2 properties.

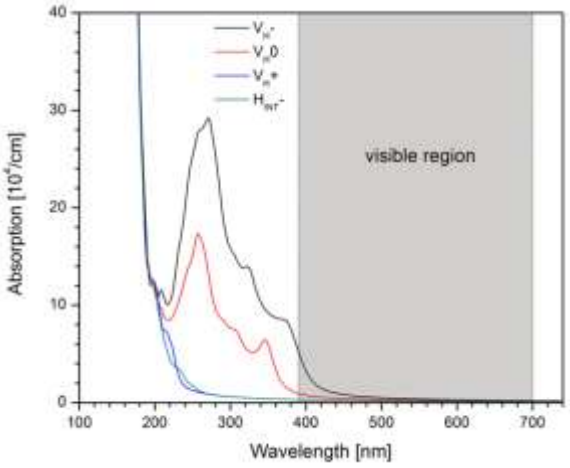

Figure 29. Wavelength dependence of absorption of MgH_2 with H-related defects. Reproduced with permission from Ž. Rašković Lovre, S. Kurko, N. Ivanović, J. F. Fernandez, J. R. Ares, S. Šturm, T. Mongstad, N. Novaković, J. Grbović Novaković, J. Alloys and Compd, 2017, 695, 2381-2388. [38]

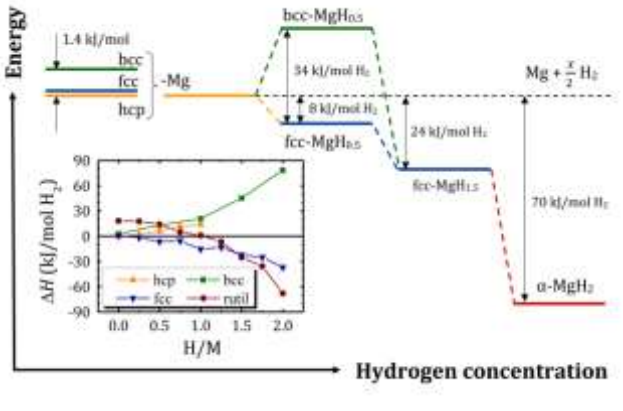

Figure 30. Energy diagram for H induced phase transformations in Mg; insert: heat of formation for various phases of MgH_x. Adapted with permission from K. Klyukin, M.G. Shelyapina D. Fruchart, *J. Alloys Comp*. 2013, *580*, S10–S12 [141].

3.5 Modelling of hydrogen induced phase transformations in magnesium and hydrogen diffusion

Another important problem that is difficult to solve experimentally is to follow the phase transformations that occur in Mg under hydrogen charging. When penetrating into hcp Mg hydrogen may occupy octahedral (O) or tetrahedral (T) sites. The hcp structure of MgH_x exists in a very narrow hydrogen concentration range [133], and the hydrogen site preference is still questionable [92,134-138]. According to recent DFT calculations [139] at low hydrogen concentrations, $x = 0.0625$, in hcp Mg the T-sites are slightly more stable: the difference between the total energy values with hydrogen in T- and O-sites is 0.08 eV; however, with hydrogen concentration increasing the O-sites became more favorable.

The theoretical studies of hydrogen induced phase transformations in Mg were reported by Tao *et al*. [136] and Klyukin *et al.* [140]. When calculating, the interstitial sites were filled in a subsequent manner to fulfill the criteria of the energy minimum. The heat of formation for hcp, bcc, fcc and rutile structures of MgH_x versus hydrogen concentration x is shown in the insert of Figure 31.

As it is shown in the energy diagram, Figure 30, in the absence of hydrogen, hcp Mg is more stable; however, already at $x \approx 0.1$ a transition to fcc-MgH_x occurs. The following H concentration increasing results in a transition to rutile-MgH_x at $x \approx 1.5$. As it is clearly seen, bcc-MgH_x is unstable in the entire range of considered hydrogen concentrations, but at low x the difference in the energy values between bcc and hcp MgH_x is not too large. It has been found that for all the studied systems [46], except bcc MgH_x [141], hydrogen, when entering into magnesium, tends to occupy neighboring interstitial sites, forming a hydride layer that prevents further penetration of hydrogen into the magnesium lattice, the so called “blocking layer effect”. In bcc-Mg it is more advantageous for hydrogen to occupy those interstitial sites, which are as far as possible from each other. Such a spreading of hydrogen over the bcc lattice, which is less compact relative to hcp and fcc lattices, may be responsible for both the increase of the hydrogen diffusion coefficient in bcc $Mg_{1-x}Nb_xH_2$ [141] compared to pure Mg and the acceleration of hydrogen sorption kinetics in Mg/Nb multilayers [142-144] and Mg-Nb (or Mg-V) composites [145,146,57]. Further theoretical modelling of hydrogen diffusion in different Mg phases [139] have supported this assumption.

Earlier studies of hydrogen diffusion in hcp-Mg reported a rather large spread of values. For example, the diffusion coefficient at 300 K, D_{hcp}(300 K), determined both experimentally [147] and theoretically [137,92] is between 4.09×10^{-13} m^2/s and 9.75×10^{-11} m^2/s. Such a large discrepancy can be explained by the difference in applied theoretical approach and/or by the fact that hydrogen diffusion is strongly affected by the hydrogen concentration and presence of defects of various natures.

Klyukin *et al.* [139,147] studied hydrogen diffusion in hcp-, bcc- and fcc-MgH_x with two hydrogen concentrations $x = 0.0625$ and 0.5. First, the preferred hydrogen interstitial sites (tetragonal T or octahedral O) were determined. Second, for all the possible hydrogen diffusion pathways, Figure 31, the activation energy,

E_a, that is the energy difference between the energy of an interstitial site (that can be global or local minimum) and the energy of a transition state between two interstitial sites, was calculated within the nudged elastic band method [148,149] accounting for zero-point energy. Finally, the hydrogen diffusion coefficient was calculated using the expression like following [139,150,151]:

$$D = n\beta L^2 \frac{k_B T}{h} e^{-\frac{E_a}{k_B T}} \left(1 + \frac{1}{2} e^{-\frac{\Delta E_{T-O}}{k_B T}}\right)^{-1} \quad (2)$$

This expression was obtained within a low temperature approximation, $h\nu \gg kT$, supposing that there is a local metastable minimum along the diffusion path, and hence, H can stay in this metastable site before another jump occurs. ΔE_{T-O} is an energy difference between the stable and metastable interstitial sites, for example, T- and O-sites, respectively; *n* is a numerical coefficient, whose value depends on the local symmetry of the interstitial site; *L* is the jump length projected onto the diffusion direction; k_B is the Boltzmann constant; h is the Plank constant; β is a parameter that can be introduce to take into account the dependence of the diffusion coefficient on the hydrogen concentration [152]. The possible H diffusion pathways as well as the calculated E_a values are shown in Figure 31.

For hcp-MgH_x the minimal E_a value corresponds to a T1→T2 jump; however, it does not correspond to any translational motion. Thus, hydrogen diffusion in hcp Mg is a many step process. For example, a possible diffusion pathway can be following: O2→T2→T1→O1→T1'→… (T1' site is situated in an adjacent unit cell). The calculated E_a value for such a complex pathway agrees well with experimental data (0.25 eV) [153], but other calculations reported by Vegge [137] and Alapati *et al.* [154] resulted in the essentially lower values. In general case, the difference between the calculated and experimental E_a values is determined, first, by the high density of defects, and second, by inhomogeneous hydrogen distribution over the metal lattice.

The hydrogen diffusion coefficient in hcp Mg at 400 °C calculated by Klyukin *et al.* [138] using equations similar to Eq. (2) was found equal to 1.07×10^{-8} m^2/s that is in fair agreement with experimental value of 2.07×10^{-8} m^2/s obtained by permeation techniques [153] and close to that one determined from molecular dynamics simulation (6.6×10^{-9} m^2/s) [92].

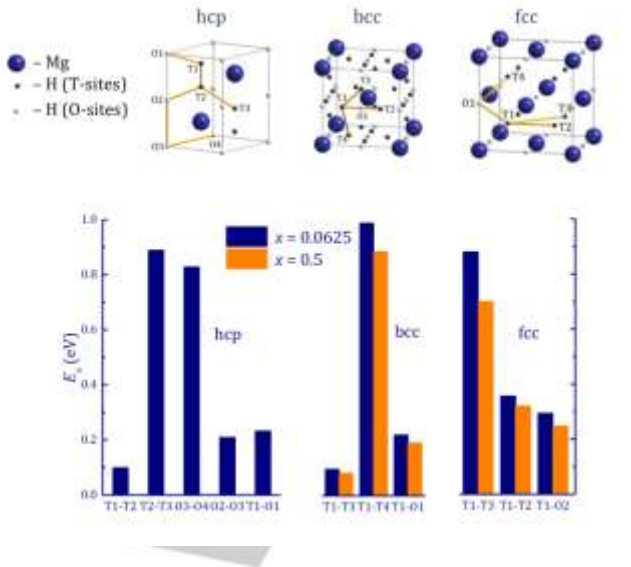

Figure 31. Possible hydrogen diffusion pathways in hcp, bcc and fcc MgH_x and corresponding activation energy values. Reproduced with permission from K. Klyukin, M. Shelyapina, D. Fruchart, *J. Alloys Comp.* **2015**, *644* 371–377 [139].

As it was mentioned above, in Mg/Nb multilayers the metastable bcc Mg structure may appears in presence of Nb. Moreover, this structure is characterized by homogeneous hydrogen distribution. The calculations of the hydrogen diffusion pathways in bcc- and fcc-Mg lattices proved that bcc-Mg exhibits the lowest activation energy for translational hydrogen motion (see figure 31) and the highest diffusion coefficient at 400 °C [139].

Summing up, theoretical studies allows us to propose the following schemes of the hydrogen induced phase transformations in magnesium [139]: hcp-Mg → hcp-MgH_x → fcc-MgH_x → rutile-MgH_2 or bcc-Mg → bcc-MgH_x → fcc-MgH_x → rutile-MgH_2, if the bcc Mg structure is stabilized. The latter can be realized either in presence of hydride forming elements with bcc structure, such as V, Nb [57], Fe [56,155], Ti-V-Cr alloys [156], FeS_2 [157] or in pure Mg subjected to sever plastic deformation (SPD) [56,61,78,158]. Violation of the regular arrangement of atoms creates conditions for destabilization of the structure, and as a result, facilitates the progress of metastable phase transition. In a sense, this situation is observed in materials subjected to SPD: SPD creates a large number of defects of different levels (one or two dimensional) that can affect the stability of the crystal structure.

3.6 Doped MgH_2

As previously stated, an obvious way to lower desorption temperature and to fasten the kinetics of the process is by mixing (typically using mechanosynthesis) with the small amount of nonmetals and metals (transition metals, their oxides, halides etc.). Whether they act as embedded dopants or catalyzers was the subject of wide scientific debate. Due to constraints imposed

by limited computing resources, the common way to deal with interaction of metals and MgH_2 was a simple doping model, with moderate dopant concentrations. This model explains the mechanism of electronic interaction, not the catalytic mechanism which functions at a much larger scale, typically at phase interfaces. There are theoretical researches; however, dealing with influence of dopants close to hydride surface and even at interfaces. Some of them will be mentioned here.

3.6.1 MgH_2 doped with boron

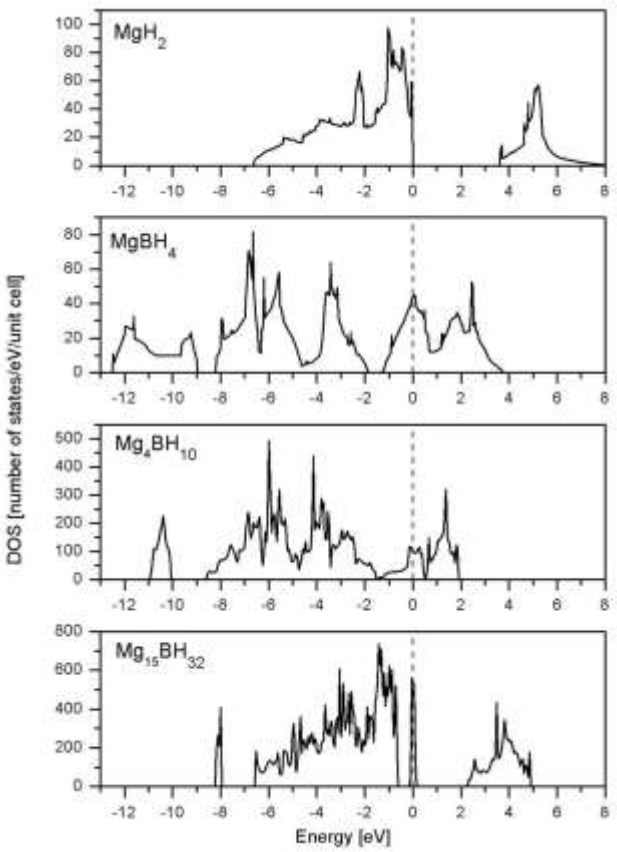

Figure 32. Densities of states of MgH_2 with Mg atom being substitutied with boron at different concentrations. Formulae corresponds (from top to bottom) to number of atoms in rutile unit cell, 5x1x1 and 2x2x2 supercells. The DOS of pure MgH_2 is presented at the top for comparison. Reproduced with permission from S. Kurko, B. Paskaš-Mamula, Lj. Matović, J. Grbović Novaković, N. Novaković, Acta Physica Polonica A 2011, 120, 238-241. [160]

Boron belongs to a class of elements that can bind significant amounts of hydrogen and release it under mild experimental conditions. Boron-based materials, specifically boron hydrides, can store up to 19% hydrogen by weight and release it at the temperatures ranging from 100 °C to 400 °C or upon chemical treatment. Another related compound, $Mg(BH_4)_2$ is typical representative of earth alkaline borohydrides and was considered as a promising candidate for the hydrogen storage due to its high gravimetric storage density (14.8 wt%) and hydrogen binding enthalpy [159]. The drawbacks of using this material for hydrogen storage are complicated and not fully reversible multiple-step desorption process, high desorption temperature and poor kinetics. The behavior of boron as substituent in MgH_2 is another approach to eventually exploit some of the electronic properties of B-H interaction.

Figure 32 shows total densities of states for MgH_2 with B acting as substitution for single Mg atom at different concentrations, decreasing from top (25 at%) to bottom (6.25 at%) [160]. DOS of pure MgH_2 is given at the top of the figure for comparison, obtained using pseudopotential method. Only the 6.25 at% system was found to be thermodynamically stable. At higher concentrations boron tends to coordinate itself tetrahedrally, resulting in considerably distorted first coordination octahedron. This distortion almost vanishes for sufficiently low concentration of boron, with almost identical, strong and short B-H bonds. The tetrahedral BH_4 arrangement is expected to exist in the vicinity of surface, in accordance with experimentally observed BH_4 ionic species in mass spectrometry during desorption [34].

3.6.2 MgH_2 doped with transition metals

There are numerous theoretical research reports concerning the nature of interaction between TMs and MgH_2 matrix in TM-doped MgH_2 systems. Chen *et al.* [161] obtained that the H-H contribution to bonding is quite small - approximately 100 times smaller than the Mg-nearest neighbor H (nnH) one and that the shortest distance between H atoms in the cluster is three times larger than in H_2 molecule. The authors have concluded that variations of ionicity are localized strictly around TM impurity and are almost TM atom independent, in strike contrast to what later calculations have shown. The main contribution to bonding was found to be ionic, while the ionic/covalent bonding ratio was determined as 7:3.

Various authors have found that local structure around TM impurities is substantially changed due to their tendency to coordinate similarly to their elemental and complex hydrides. Dai *et al.* have found that Ti prefers both substitutional and interstitial sites, while Mn and Ni interstitial sites near the surface of MgH_2 [132,162]. Ti alters its surrounding profoundly with the tendency to form the local structural arrangement like the one in stable TiH_2 hydride. Mn tends to form Mn-H clusters with the structure similar to the one of Mg_2MnH_7, while Ni forms regular NiH_4 tetrahedrons, as the precursors for the formation of the Mg_2NiH_4 phase.

Er *et al.* [163] have shown that for TM (TM = Sc, Ti, V and Cr) concentration approaching x = 0.2 in $Mg_xTM_{1-x}H_2$ (much higher than those used in this work), the fluorite structure with cubic H environment becomes more stable than the rutile one. The charge of TM and its nearest neighbor H atoms in these compounds is weakly influenced by Mg and the particular crystal structure (rutile or fluorite), again in contrast to more recent calculations. Song *et al.* [164] have reported somewhat improved H sorption thermodynamics of Ti doped system.

Vegge *et al.* [165] have calculated some simpler crystal structures of MgTM (TM = entire 3d series) alloys and of their hydrides $MgTMH_3$, with focus on electronic trends. In this paper, calculated enthalpies of formation revealed a gradual increase of the MgTM hydrides stability going from Sc to Fe, followed by a rapid decrease, causing $MgNiH_3$ to be only marginally stable and $MgCuH_3$ and $MgZnH_3$ unstable. The two contributions to TM-H cohesion have been found: the attractive one originating from the downshift of the occupied bonding H(1s)-TM(3d) state and the repulsive one, increasing with the gradual filling of the antibonding states from $MgMnH_3$ to $MgZnH_3$. Giusepponi and Celino [166] have found that the interface adhesion energy and mobility of near surface hydrogen atoms are the decreasing functions of iron dopant distance from surface.

Substitution effects are usually accompanied by a decrease in local symmetry. From this perspective the more flexible cluster approach can be used to study MgH_2-TM systems. In addition, it can be applied to investigate the size effect on physical and chemical properties of nanoparticles. Wagemans *et al.* [167] studied Mg_nH_{2n} clusters with n ≥ 56. According to their calculations, Mg_nH_{2n} clusters with n < 10 should exhibit lower stability as compared to bulk α-MgH_2, Figure 33. For instance, for a Mg_9H_{18} cluster with size of 0.9 nm a hydrogen desorption enthalpy of 63 kJ/mol·H_2, which corresponds to desorption temperature of 200 °C, was predicted.

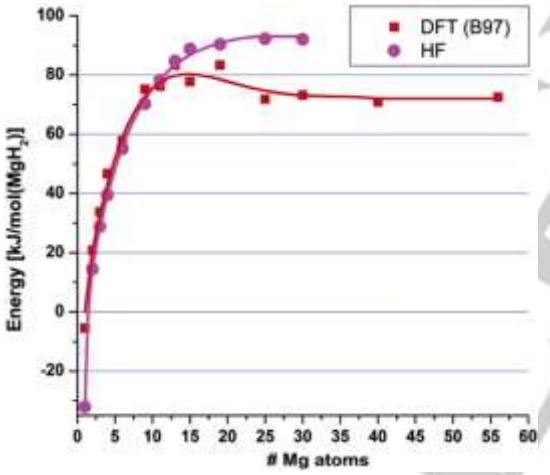

Figure 33. Calculated desorption energies for MgH_2 clusters with both the Hartree-Fock (HF) method and DFT method (B97 functional). The energies are normalized per mole of H_2 released. Reproduced with permission from R. W. P. Wagemans, J. H. Van Lenthe, P. E. De Jongh, A. J. Van Dillen and K. P. De Jong, *J. Am. Chem. Soc.* **2005**, *127*, 16675–16680 [167].

However, Mg_nH_{2n} clusters with n < 19 have a rutile-like structure and exhibit desorption energy similar to that of bulk MgH_2. The results obtained by Wagemans *et al.* [167] looks rather promising, nevertheless, in practice the synthesis of Mg nanoparticles of few nanometer sizes is a challenging task. Ball milling provides the minimal particle size of 500 nm that improves hydrogen sorption kinetics but not the thermodynamic stability. Further decrease in particle size is limited due to agglomerations and cold welding during the milling process [160]. Mg nanoparticles of < 5 nm size can be obtained by infiltration of nanoporous carbon with molten magnesium [169] or by electrochemical synthesis [170]. As it was predicted [167], they absorb hydrogen at near room temperature, and the corresponding hydrides desorb hydrogen at 165 °C, but the synthesis method is not appropriate for industrial production.

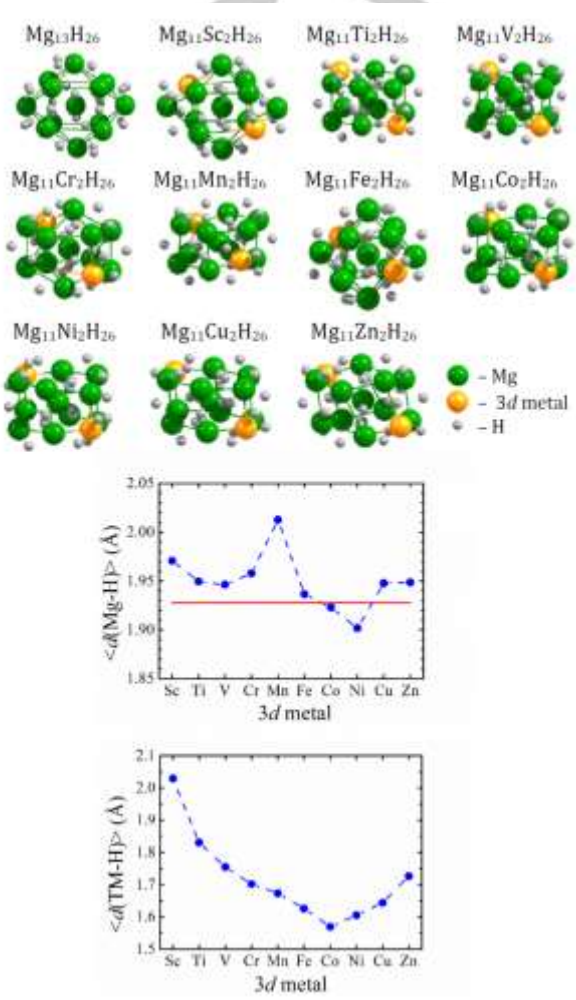

Figure 34. Optimized structures of the non-substituted $Mg_{13}H_{26}$ and substituted $Mg_{11}TM_2H_{26}$ clusters TM = Sc, …,Zn and the averaged Mg–H, TM–H distances. The solid horizontal line represents the averaged Mg–H distance in $Mg_{13}H_{26}$. Adapted with permission from M. G. Shelyapina and M. Y. Siretskiy, *Phys. Solid State*, **2010**, *52*, 1992–1998 [173].

The impact of TM additives on MgH_2 stability within the cluster approach was studied in several works [171-173]. Larsson *et al.* [171] studied $(MgH_2)_{31}$ clusters with an Mg atom substituted for TM = Ti, V, Fe, or Ni. It was obtained that considered TM atoms exhibit rather different site preferences. A wider set of transition elements (TM = Sc … Zn) was studied in references [172,173] using a $Mg_{13}H_{26}$ cluster model that represents a fragment of the bulk Mg_7TiH_{16} hydride. It was found that for a non-substituted

$Mg_{13}H_{26}$ cluster the interatomic distances, the gap between the highest occupied and the lowest unoccupied molecular orbitals) and the enthalpy of hydride formation are close to those for bulk MgH_2. A partial substitution of Mg for TM leads to a distortion of the shape of the cluster, less pronounced for TM = Sc, and increase in the Mg–H distances (except for TM = Co and Ni), Figure 34.

The analysis of the TM–H bond lengths demonstrated that hydrogen is strongly bound to the 3*d* metal atoms. A comprehensive analysis showed that Sc, Ti, Cu, and Zn are the most promising additives to MgH_2 in terms of hydrogen storage. In general, the results obtained within this cluster approach are in coherence with those of bulk calculations.

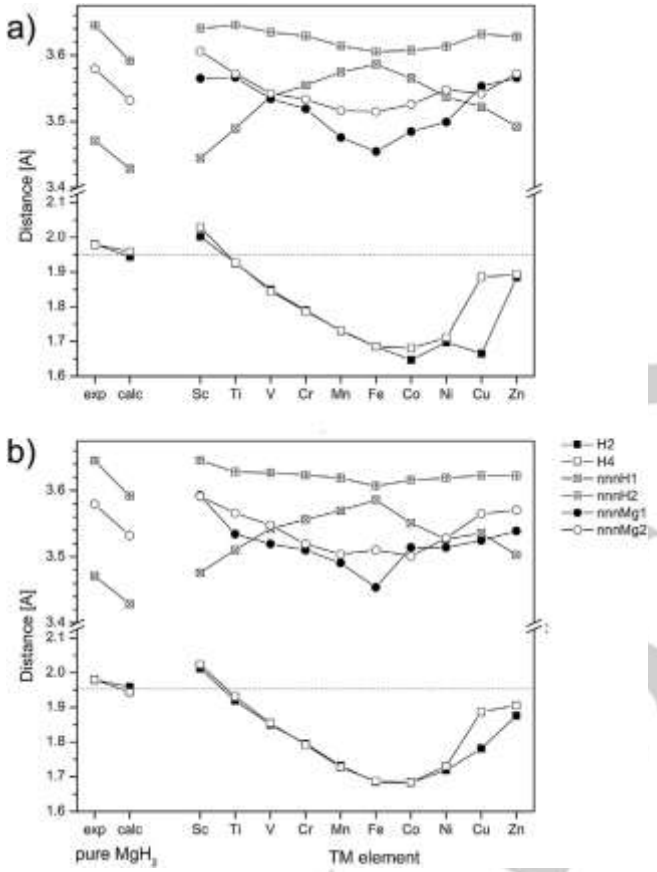

Figure 35. Calculated distances from TM to atoms in the several nearest coordination shells for the entireMgH_2:TM series. Reproduced with permission from B. P. Mamula, J. G. Novaković, I. Radisavljević, N. Ivanović, N. Novaković, Int. J. Hydrogen Energy, 2014, 39(11), 5874-5887 [106]).

The results of bulk structural relaxation of the entire MgH_2:TM series is presented in Figure 35 [106]. The experimental and calculated Mg-H nearest neighbor distances in pure MgH_2 are given for comparison and marked with horizontal dashed line. The distances are proportional to calculated charge densities in bCP points along TM-H bonding path. In the same work, the trend in calculated excess charges (integrated over atomic basins) indicates an increase of open shell interactions share in the total TM-H cohesion compared to predominantly ionic nature of Mg-H bonding in pure MgH_2. The trend in bCP charge density is compensated in second and almost completely absent in the third shell of TM coordination, which render the doping effect to be very local.

The density of states (DOS) of MgH_2 doped by TM also exhibits rather common features. Figure 36 schematically shows the changes in DOS that appear when Mg is partly substituted for a TM atom [174]: MgH_2 is an insulator with an energy gap of about 4 eV, Figure 36a; however, alloying with TM atoms results in appearance of a narrow *d*-band in the middle of the gap with the Fermi level (E_F) within [176-179,104]. For TM = Sc or Ti this band is almost empty and E_F is at the bottom edge of the band, Figure 36b, with further *d*-band filling E_F shifts towards the top edge of the *d*-band, Figure 36c, and finally is completely filled for TM = Zn, figure 36(d). As it was shown by Shelyapina *et al.* [176], the *d*-states of TM are hybridized with *s*-states of hydrogen atoms that points out to a strong bonding between TM and H.

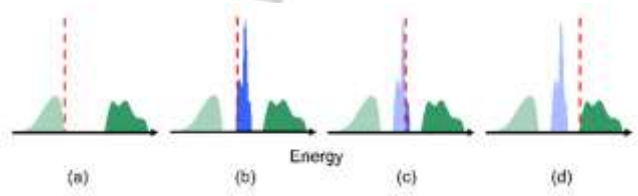

Figure 36. A schematic representation of the impact of alloying TM atoms on the DOS in MgH_2: (a) – DOS for pure MgH_2, (b-d) for MgH_2+TM with gradual filling of the *d*-band. Vertical dashed line represents E_F. Reproduced with permission from M.G. Shelyapina, D. Fruchart, Solid State Phenom. **2011**, *170*, 227–231 [174].

The bond weakening between Mg and H atoms in MgH_2 with Mg partially substituted for TM is more evidenced from the electron density maps, Figure 37. However, a rather strong TM–H bonding limits further decreasing stability of MgH_2–TM, and as a result, the decreasing of hydrogen desorption temperature [176]. A possible solution to overcome this problem is a partial substitution of Mg for atoms that, on the one hand, would form stable compounds with both Mg and TM, and on the other hand would form metastable hydrides. As shown in Ref. [177] for Mg_6TiAl and Mg_6TiZn and their hydrides substitution of Mg for Al or Zn leads to stabilization of the alloys with simultaneous decreasing stability of the corresponding hydrides due to the TM–H bond weakening, see Figure 37.

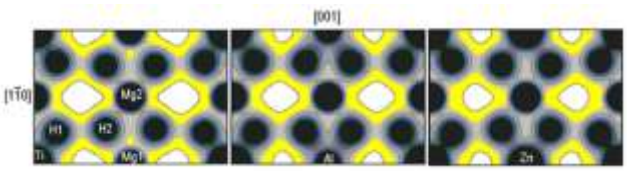

Figure 37. Electronic density maps for Mg_7TiH_{16} (left), Mg_6TiAlH_{16} (centre) and Mg_6TiZnH_{16} (right) hydrides in the (110) plane. Adapted with permission from

M. G. Shelyapina, D. Fruchart, S. Miraglia, G. Girard, *Phys. Solid State* **2011**, *53*, 6–12, [177].

Dominant role of ionic bonding in the TM-H interaction for TMs from the beginning (Sc, Ti) and the end (Cu, Zn) of the series is depicted by high values of Bader excess charge and low values of bCP charge density. Indications of significant contribution of open-shell bonding for Mn, Fe and Co are low values of Bader excess charge, high values of bCP charge density and quite a good agreement between the covalent radii-based and calculated TM-H distances. The observed reverse of the trend in bond length and bCP and excess charges can be explained by the details of electronic structure and the filling of antibonding states starting from the middle of TM series.

RDG plots for the first coordination polyhedron of transition metal (TM) impurities Ti, Fe i Cu atom in MgH_2:TM compared to pure MgH_2 are presented in Figure 38.

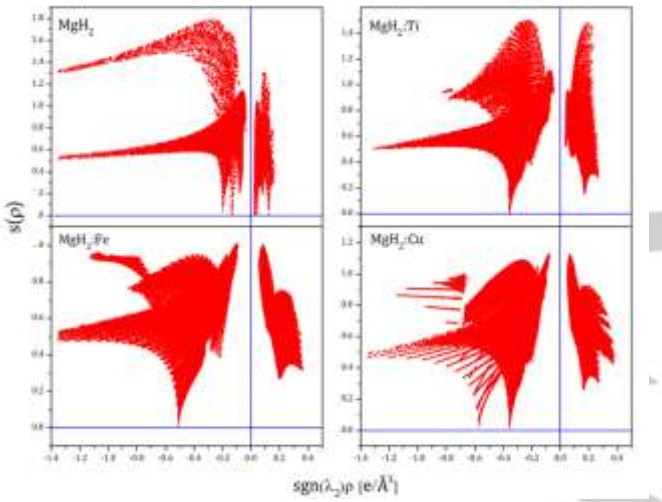

Figure 38. Reduced gradient density plots as a function of $sgn(\lambda_2)\rho$ in the first coordination polyhedron of Mg atom in pure MgH_2 and Ti, Fe and Cu atoms in MgH_2:TM.

Comparing peaks on the negative side of $sgn(\lambda_2)\rho$ in MgH_2 and those in systems with TM impurity, it is clear that first coordination of TM is much simpler. The only identified interaction is between TM-H nearest neighbor atoms, in accordance with results of QTAIM analysis. Higher values of charge density matching NCI peaks in the bonding region in MgH_2:TM systems are a consequence of a larger contribution of interactions characteristic for open shell systems. This is an explanation for absence of interactions between H atoms in the first coordination of TM impurity.

While charge density of the only attractive peak rises from Ti to Fe, the situation is somewhat different in case of Cu. Appearance of two distinct peaks on the negative side of the x-axis for Cu and the fact that the largest value of charge density matches the lower peak are a consequence of significant distortion of the first coordination polyhedron of this TM. Cu-H2 bond length is among the shortest observed between TM and H atom for all 3d metals. Non-interacting charge density region along the direction connecting closer H atoms in the second coordination around TM to a certain extent exists in the case of Fe and are almost completely absent for all the other transition metals which is in sharp contrast to situation in pure MgH_2.

NCI isosurfaces in the first coordination polyhedron of TM atoms for different values (Figure 39) are more diffuse compared to the ones around an Mg atom in MgH_2. For low *s* values, regions in MgH_2 and doped systems resemble, although regions around *bcp*(TM-H) are expectedly larger. Outside of the directions connecting TM and its first neighbours there are not many details, in accordance with the fact that critical points between second neighbors within the first PM coordination do not exist.

For larger values or reduced charge density, the situation becomes more complicated, as a result of the redistribution of a larger amount of charge, which has been taken into account and the way in which this redistribution includes bonding, non-bonding and antibonding states that are filled along the TM series. Although detailed analysis of NCI plot is a complex task, the pronounced difference between pure and doped MgH_2 can be explained by distribution in TM-H bonds and ascending contribution of open-shell interaction in doped systems.

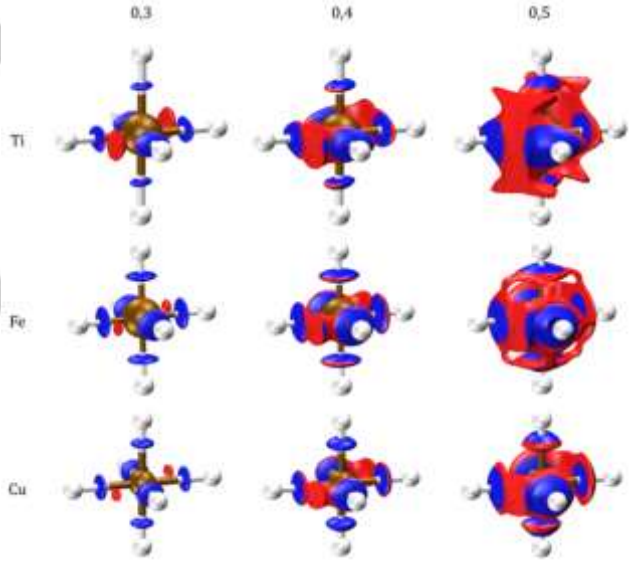

Figure 39. NCI isosurfaces in the first coordination polyhedron of Ti (top), Fe (middle) and Cu (bottom) atom in MgH2:TM. Golden central sphere is TM atom and white ones are H atoms. From left to right values of s(ρ) are 0.3, 0.4, 0.5.

3.6.3 Body centred cubic magnesium stabilized in Mg/Nb multilayers: theoretical studies and experimental evidences

Numerous studies have explored that hydrogen sorption kinetics of magnesium may be improved by several ways, for example, by mixing magnesium or magnesium hydride with niobium

[180,103,145,142,46]. As magnesium does not form any bulk compound or binary alloy with Nb the issue of this phenomenon is not completely understood.

In situ X-ray diffraction studies of dehydration process in MgH_2-Nb nanocomposites done by Pelletier *et al.* [180] helped a lot to expose mechanisms that are responsible for improvement of hydrogen sorption kinetics by Mg in presence of Nb. They have revealed that hydrogen penetrates and diffuses into Mg through the Mg/Nb interfaces forming intermediate metastable NbH_x hydrides [180]. Further studies of Mg/Nb multilayers [142] and a Mo/Mg/Nb/Pd/Mo/Al_2O_3 "nano tank" [143] have confirmed this result. It implies that Nb nanoparticles or thin deposits act not as a true catalyst but as a gateway for hydrogen delivery to Mg [180,143,144]. This experimentally obtained evidence stimulated theoretical studies of Mg/Nb multilayers and Mg/Nb interfaces in particular.

Theoretical approaches mainly based on application of density functional theory and done for both bulk [107,175-178,181] and nanoparticles [161,172-174,182] have proved themselves as a powerful tool to reveal issues of the decreasing MgH_2 stability when alloying Mg with transition metals (TM), including Nb: alloying TM leads to weakening bonding between H and Mg atoms with simultaneous increasing of TM–H bonding [174,176]. The latter limits further improvement of the hydrogenation and dehydrogenation properties of the ternary magnesium based hydrides [176,177]. Nevertheless, simulations of Mg/TM multilayers, as well as of the theoretical studies of the impact of TM additives on improvement of hydrogen sorption kinetics have not been so numerous until recently.

Klyukin *et al.* [183] considered various structural models of Mg_4/Nb_4 and Mg_6/Nb_2 multilayers: Mg(bcc)/Nb(bcc) staked in bcc-(011) plane, Mg(hcp)/Nb(hcp) staked in hcp-(0001) plane, and Mg(hp)/Nb(bcc) for which Mg hcp-(0001) structure was staked on Nb bcc-(011). These crystallographic planes were considered to model Mg/Nb interface as they exhibit the highest reticular density and hence must be the most favorable in term of metallic bonding. However, it should be noted that for hcp Mg-(0001) and bcc Nb-(011) the lattice mismatch Δ, determined as $\Delta = 100\% \cdot (a_s - a_f)/a_f$, where a_s is the lattice parameter of the substrate and a_f is the lattice parameter of the deposed layers, is about 9%, that must cause rather high internal strain. The optimization of the structure for the bulk bcc-Mg results in 7.7% of the lattice mismatch between bcc-Mg and bcc-Nb. Nevertheless, according to the studies reported in Ref. [183], in thin multilayers magnesium may adopt the bcc structure of niobium, with lattice parameter close to the bcc-Nb one.

It should be noted that the bcc structure of Mg can be stabilized at high pressure [134]. Calculations of the Burger's transformation path hcp ↔ bcc in the Mg lattice showed that at first the sheer deformation dominates but at the end of transformation the slide displacement becomes stronger [140], see Figure 40. The theoretical study of fully relaxed and constrained bcc-Mg lattices done by Junkaew *et al.* [184] proved that metastable bcc-Mg structures can be stabilized either under high hydrostatic pressure or constraints arising from interfacial interactions between Mg and Nb. The latter are important in nanoscale systems and can contribute to the stabilization of metastable phases in thin films [184,185]. For example, metastable $Mg_{1-x}Nb_x$ alloys ($0.25 \le x \le 0.31$) with bcc structure can be obtained in the form of thin films [133].

The structure of multilayers is governed by many factors, including the film thickness and the number of atomic layers. Kumar *et al.* [186] have theoretically predicted that a coherent bcc-Mg/Nb interface can be formed when Mg layer is less than 4.2 nm. Increasing the Mg layer thickness should result in emerging of a semi-coherent hcp-Mg/Nb interface.

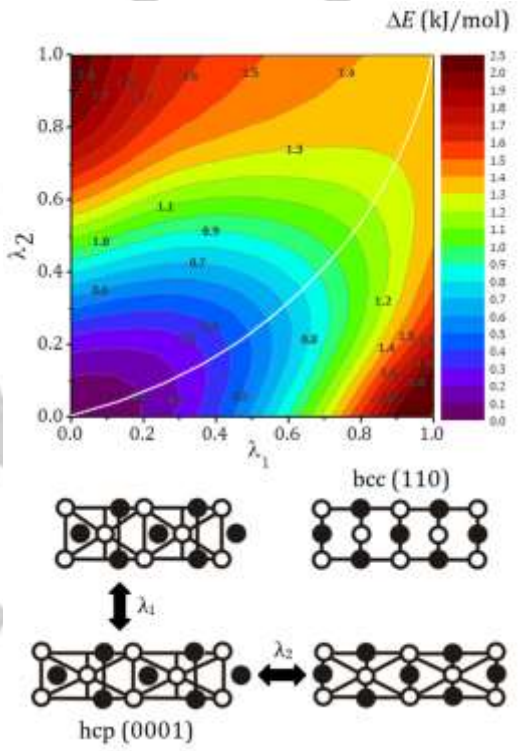

Figure 40. Contour plot for the potential surface of the Burgers hcp ↔ bcc phase transition in Mg; the solid line shows the energy efficient transition pathway. Adapted with permission from K. Klyukin, M.G. Shelyapina D. Fruchart, *J. Alloys Comp*. 2013, *580*, S10–S12. [140]

These theoretical results have been proved experimentally [184,187,188]. Ham *et al.* [187] have shown that the bcc-Mg structure may appear in Mg/Nb multilayers under ambient conditions. Pathak *et al.* [188] have demonstrated that in 5 nm/5 nm Mg/Nb multilayers both phases adopted the same bcc lattice parameter <*a*> = 0.3347 nm, whereas in 50 nm/50 nm multilayers the lattice parameters of Mg and Nb layers are similar to those of bulk. In addition, Mg/Nb multilayers of a few nanometers thickness exhibit essentially higher mechanical strength as compared to bulk magnesium [187,188].

Thereby, one can conclude that due to interfacial interactions between Mg and Nb metastable bcc-Mg structure can be stabilized in Mg/Nb thin films or multilayers when the Mg layer thickness is below 5 nm. The question whether this bcc phase

may appear in Mg-Nb nanocomposites exposed to ball milling or other actions is still debatable and need deeper research.

3.6.4 MgH_2 doped with oxide ceramics

A large number of experimental studies confirm that the addition of metal oxides, such as TiO_2, Al_2O_3, VO_2 and V_2O_5, Nb_2O_5 and Fe_3O_4, has beneficial effect on destabilization of MgH_2 matrix and cause improvement of kinetic properties of this material [50,100,189-191]. Among the various metal oxides used as catalysts, TiO_2 is noteworthy because it has low cost and high availability, besides its great catalytic characteristics [192]. Even though a large number of authors claim the catalytic activity of both Ti and TiO_2 to enhance the (de)sorption of hydrogen in MgH_2 the atomic-scale role of them is far from clear. As shown by Jung *et al.* [190] addition of only 5 mol% of rutile TiO_2 significantly improved hydrogen absorption kinetics. Pandey *et al.* [193] have obtained the lowest hydrogen desorption activation energy is for 50 nm TiO_2 particles. According to Croston *et al.* [191] a reduction of the Ti^{+4} in TiO_2 to metallic Ti appears to result in the formation of the active species responsible for catalyzing the MgH_2 dehydrogenation reaction.
Concerning the surface TiO_2-H interaction, Yin *et al.* [194] have obtained the maximum H monolayer coverage on TiO_2 (110) surface of only 70% at room temperature, regardless of the applied partial pressure of hydrogen. The same author confirmed that during the heating of the hydrogenated sample, H atoms have migrated into TiO_2 bulk – an unusual behavior, since desorption of H_2 (or H_2O) molecules into the gas phase is a common characteristic of hydroxylated oxide surface. These results were confirmed by other authors [195]. Filippone *et al.* [196] carried out research which showed that hydrogen behaves as a deep donor in rutile phase. They have also shown that electronic localization effects in the bulk TiO_2 call for the addition of the Hubbard-like term to properly describe bonding and changes in charge distribution after hydrogen incorporation. Moreover, the formation of Ti^{+3} species due to the localization of H and OH+ electronic levels on some Ti neighbors, supports the idea that hydrogen atoms are adsorbed as protons onto outer oxygen atoms.
As shown by microstructural analysis provided by Cui *et al.* [55], nano-sized layer of TiO_2 with nano-grains of less than 10 nm covers the surface of Mg. In this kind of structure, multiple-valence Ti not only acts as a catalyst but also forms many interfaces with Mg/MgH_2.

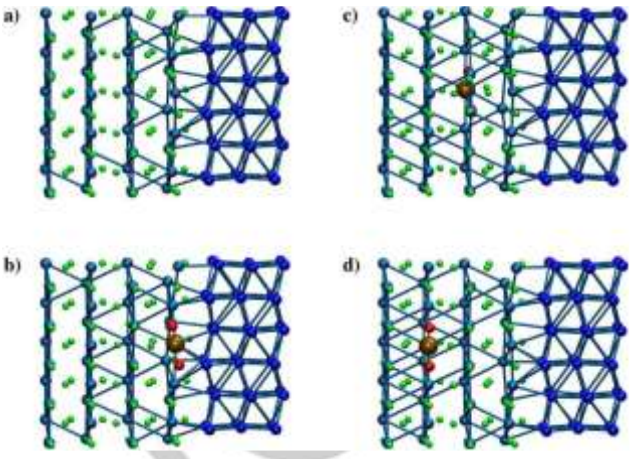

Figure 41. MgH_2/hcp Mg interface models used in calculations. Brown and red balls represent embedded Ti and O atoms near interface in different atomic layers. Blue spheres – Mg, green – H, gold – Ti and red – O. Reproduced with permission from R. Vujasin, J.Grbović Novaković, N. Novaković, S.Giusepponi, M.Cellino, Journal of Alloys and Compounds 696, 2017, 548-559 . [197]

In the study by Vujasin *et al.* [197] the properties of MgH_2/Mg interface have been investigated - the diffusion of H in the vicinity of Ti and TiO_2 species embedded close to hydride/metal phase boundary has been assessed using Car-Parinello molecular dynamics and Bader QTAIM charge analysis. The interface model has been chosen based on work of adhesion optimization (see Figure 41). Ti and TiO_2 have been embedded in different atomic layers parallel and close to phase boundary. Molecular dynamics has shown that mobility of H on the interface is increased in the vicinity of Ti and reduced in the vicinity of TiO_2. At the same time, TiO_2 did not show any sign of dissociation, meaning that O atoms stay firmly bounded to Ti. Structural results and Bader charge analysis showed that in the presence of more electronegative O atoms, first neighbor H atoms accept less charge from Mg than in the case of pure MgH_2. As a consequence, they form shorter bonds with central Ti atom, which can explain to some extent why the mobility of H is reduced close to TiO_2 species.

4. Conclusions

This review deals with destabilization methods for improvement of storage properties of metal hydrides. Both theoretical and experimental approaches were used to emphasize the influence of various types of defects on structure and stability of Mg-based hydrides. As a case study, Mg based hydrides has been investigated. The influence of ion irradiation and mechanical milling with and without additives has been discussed. Ion irradiation is the way to introduce a well-defined concentration of defects (Frankel pair) at the surface and sub-surface layer of a material. Defects at the surface play the main role in sorption reaction since they enhance the dissociation of hydrogen. On the other hand, ball milling introduces defects through all the

sample volumes, refine the structure thus decrease the path for hydrogen diffusion. Two Severe Plastic Deformation techniques were used to better understand the hydrogenation/ dehydrogenation kinetics of Mg- and Mg_2Ni-based alloys, being respectively Equal-Angular-Channel-Pressing and Fast-Forging.
Successive ECAP passes leads to refine the microstructure of AZ31 ingots and install therein high densities of defects. Depending on mode, number and temperature of ECAP passes, the H-sorption kinetics have been improved satisfactorily without any additive for mass H-storage applications considering the relative fastness of the shaping procedure. A qualitative understanding of the kinetic advance principles has been built.
Fast-Forging was used for a “quasi-instantaneous” synthesis of Mg/Mg_2Ni-based composites. Hydrogenation of the as-received almost bi-phased materials remains rather slow as generally observed elsewhere whatever are multiple and different techniques used to deliver the composite alloys. However, our preliminary results suggest that a synergic hydrogenation / dehydrogenation process should assist hydrogen transfers from Mg/Mg_2Ni on one side to MgH_2/Mg_2NiH_4 on the other side via the rather stable a-$Mg_2NiH_{0.3}$, acting as *in-situ* catalyser.
Theoretical studies, mainly carried out within various realizations of DFT, are proved to be a powerful tool to study MgH_2 based materials. Providing an insight on metal-hydrogen bonding, that governs both thermodynamics and hydrogen kinetics, they allow us to describe phenomena, to which experimental methods have a limited access or do not have it at all: to follow the hydrogen sorption reaction on a specific metal surface and hydrogen induced phase transformations, to describe structure of phase boundaries, to explain the impact of defects or various additives on MgH_2 stability and hydrogen sorption kinetics. In several cases theoretical calculations reveal themselves able to predict new properties of materials, including the ways to modify Mg or MgH_2 that would lead to better characteristics in terms of hydrogen storage.
Beside prevalently ionic first neighbour interaction, charge density analysis of bonding in pure MgH_2 reveals non negligible contribution of second neighbour H-H interaction as well.
It is shown that the mobility of H atoms and/or H vacancies is heavily dependent on H surface concentration. In other words, it is of vital importance to find an efficient way of removing surface hydrogen (H_2 recombination or some competitive process) in order to enable fast diffusion toward phase boundary and desorption of H. The calculations also show that substoichiometric Mg hydride present during (de)sorption process and the infleunce of H vacancies on electronic structure could be the explanation for observed changes in colour of MgH_2 thin films.
The effects of substitution of Mg with boron are dependent on concentration and the vicinity if surface or site symmetry reduction. B tends to coordinate itself tetrahedrally and the nature of bonding is shifted toward open-shell interactions.
The systematical bulk and cluster investigation of substitution of Mg with 3d transition metals reveals locally stronger and shorted TM-H bonds which in turn weakens the rest of the host matrix. The trends of bond length and strength can be attributed to peculiarities of localized narrow 3d states within energy gap. It is shown that additional substitution of Mg atoms with atoms f metastable hydrides (Al, Zn) can further decrease the stability of the system and thus improve sorption properties.
Calculations of influence of metal and its oxide close to metal-hydride interfaces revealed that hydrogen mobility is reduced in the presence of oxide, not in accordance with experimental findings. This could be attributed to the limitations of the proposed calculation model.

Acknowledgements

This paper is financially supported by Serbian Ministry of Education and Science under grants III45012, III45018 and 171001. The authors are also grateful to the Resource Center «Computer Center of SPbU» (http://cc.spbu.ru/en) for providing computational facilities.

Keywords: hydrides, ab initio calculations, material science, energy conversion

[1] L. Schlapbach, A. Zuttel, *Nature* **2001**, 414, 353-358.
[2] Materials Challenges in Alternative and Renewable Energy, edited by George Wicks, Jack Simon, Ragaiy Zidan, Edgar Lara-Curzio, Thad Adams, Jose Zayas, Abhi Karkamkar, Robert Sindelar, Brenda Garcia-Diaz, *Ceramics Transactions Volume 224*, John Wiley & Son, ISBN 987-1-1180-1065-3, **2011.**
[3] F. Ding, B. I. Yakobson, *Front. Phys.* **2011**, 6(2), 142–150.
[4] R.Balderas-Xicohténcatl, M. Schlichtenmayer, M. Hirscher, *Energy Technology* , **2018**, 6(3), 578-582.
[5] H.W.Langmi, J.Ren, B.North, M.Mathe, D.Bessarabov, *Electrochimica Acta* **2014**, 128, 368-392.
[6] Y. Xia, Z. Yang, Y. Zhu, *J. Mater. Chem*. A **2013**, 1, 9365-9381.
[6] J. Huang, Y.Liang, H. Dong, H. Hu, P. Yu, L. Peng, M. Zheng, Y. Xiao, Y. Liu, Int. *J. Hydrogen Energy* **2018**, 43(39), 18077-18082.
[7] J. Weitkamp, M. Fritz and S. Ernst, *J. Hydrogen Energy* **1995**, 20(12), 967- 970.
[8] A. Martin-Calvo, J.-J. Gutiérrez-Sevillano, I. Matito-Martos, T. J. H. Vlugt, and S. Calero, *J. Phys. Chem. C* **2018**, 122 (23), 12485–12493.
[9] P.K. Chattaraj,S. Bandaru, S. Mondal, *J. Phys. Chem. A* **2011**, 115 (2), 187–193.
[10] H. Prakash Veluswamy, R. Kumar, P.Linga, *Applied Energy* **2014**, 122, 112–132.
[11] N. Biliškov, A. Borgschulte, K. Užarević, I. Halasz, S. Lukin, S. Milošević, I. Milanović, J. Grbović Novaković, *Chemistry–A European Journal* **2017**, 23(64), 16274-16282.
[12] H.Chu, S. Qiu, L.Sun, F.Xu, *Storage and Utilization Chapter 3* **2015**, doi.10.5772/61048, 53-59.
[13] J.Jepsen, C. Milanese, J. Puszkiel, A. Girella, B. Schiavo, G. A Lozano, G. Capurso, J.M.B Von Colbe, A.Marini, S. Kabelac,M. Dornheim, T. Klassen, *Energies* **2018**, 11(5), Article number 1081.
[14] G. Moussa, R. Moury, U. B. Demirci, T. Şener, P. Miele, *Int.J Energy Res.* **2013**, DOI:10.1002/er.3027.
[15] Lj. Matović, N. Novaković, S. Kurko, M. Šiljegović, B. Matović, Z. Kačarević Popović, N. Romčević, N. Ivanović, and J. Grbović Novaković, *Int. J. Hydrogen Energy* **2009**, 34, 7275-7282.
[16] J. Grbović Novaković, Lj. Matović, M. Drvendžija, N. Novaković, D. Rajnović, M. Šiljegović, Z. Kačarević Popović, S. Milovanović, and N. Ivanović, *Int. J. Hydrogen Energy* **2008**, 33, 1876-1879.

[17] H. Uchida, *Int. J. Hydrogen Energy* **1999**, 24, 861-869.
[18] Á. Révész, M. Gajdics, E. Schafler, M. Calizzi, L. Pasquini, *J. Alloys Compd.* **2017**,702, 84–91.
[19] M. Zhu, Y. Lu, L. Ouyang, H. Wang, *Materials* **2013**, 6, doi:10.3390/ma6104654, 4654-4674.
[20] Y. Adda, M. Beyeler, G. Brebec, *Thin Solid Films* **1975**, 25, 107-156.
[21] J. S. Williams, J. M. Poate in *Ion Implantation and Beam Processing*, Academic Press, New York, **1984**.
[22] P. Sigmund in *Fundamentals Processes in Sputtering of Atoms and Molecules*, Medd. Kgl. Dan.Vindensk (Royal Danish Academy of Sciences and Letters, Copenhagen), **1992**.
[23] H. Ehrenreich, F. Spaepen in *Solid State Physics*, Academic Press, New York, **1998**.
]24] Y. Chimi, K. Adachi, A. Iwase, N. Ishikawa, K. Yamakawa, *J. Alloys Compd.* **2002**, 330, 187-190.
[25] M. Nastasi and J. W. Mayer in *Ion Implantation and Synthesis of Materials*, Springer-Verlag, Berlin Heidelberg, **2006**.
[26] H. Abe, R. Morimoto, F. Satoh, Y. Azuma, H. Uchida, *J. Alloys Compd.* **2005**, 404, 288-292.
[27] H. Abe, R. Morimoto, F. Satoh, Y. Azuma, H. Uchida, *J. Alloys Compd.* **2006**, 408, 348-350.
[28] H. Abe, S. Aone, R. Morimoto, H. Uchida, *J. Alloys Compd.* **2013**, 580, S219-S221.
[29] H. Uchida, S. Kato, *J. Alloys Compd.* **2006**, 408, 319-322.
[30] H. Uchida, K. Yamashita, T. Tabata, H.H. Uchida, M. Iwase, Y. Katoh, *J. Alloys Compd.* **1999**, 293, 751-755.
[31] H. Abe, S. Tokuhira, H. Uchida, T. Ohshima, *Nucl. Instrum. Methods Phys. Res.* **2015**, B 365, 214-217.
[32] J.F. Ziegler in *The Stopping and Range of Ions in Matter*, Pergamon Press, New York, **1985**.
[33] A. López-Suárez, C. E. Valencia, J. López-Patiño, M. C. Vargas, B. E. Fuentes, *Int. J. Hydrogen Energy* **2015**, 40, 4194-4199.
[34] S. Kurko, Lj. Matović, N. Novaković, B. Matović, Z. Jovanović, B. Paskaš Mamula, J. Grbović Novaković, *Int. J. Hydrogen Energy* **2011**, 36, 1184–1189.
[35] S. Kurko, I. Milanović, S. Milošević, Ž. Rašković-Lovre, J. F. Fernandez, J. R. Ares Fernandez, Lj. Matović, J. Grbović Novaković, *Int. J. Hydrogen Energy* **2013**, 38, 12199-12206.
[36] J. Grbović Novaković, S. Kurko, Ž. Rašković-Lovre, S. Milošević, I. Milanović, Z. Stojanović, R. Vujasin, Lj. Matović, *Mater. Sci. (Medžiagotyra)* **2013**, 19, 134-139.
[37] Lj. Matović, S. Kurko, Ž. Rašković-Lovre, R. Vujasin, I. Milanović, S. Milošević, J. Grbović Novaković, *Int. J. Hydrogen Energy* **2012**, 37, 6727-6732.
[38] Ž. Rašković Lovre, S. Kurko, N. Ivanović, J. F. Fernandez, J. R. Ares, S. Šturm, T. Mongstad, N. Novaković, J. Grbović Novaković, *J. Alloys and Compd*. **2017**, 695, 2381-2388.
[39] A. Zaluska, L. Zaluski, J.O. Ström-Olsen, *J. Alloys Compd.* **1999**, 288, 217-225.
[40] R.A. Varin, M. Jang, T. Czujko, Z.S. Wronski, *J. Alloys Compd.* **2010**, 493, L29-L32.
[41] A. Bassetti, E. Bonetti, L. Pasquini, A. Montone, J. Grbovic, M.V. Antisari, S. Amadori, E. Bonetti, E. Callini, A.L. Fiorini, A. Montone, M. Vittori Antisari, *Eur. Phys. J. B* **2005**, 43, 19-27.
[42] R.A. Varin, T. Czujko, Z. Wronski, Nanotechnology 2006, 17, 3856.
[43] I. Milanović, S. Milošević, Ž. Rašković-Lovre, N. Novaković, R. Vujasin, L. Matović, J. Francisco Fernández, C. Sánchez, J. Grbović Novaković, *Ceram. Int.* **2013**, 39, 4399-4405.
[44] C. Suryanarayana in *Mechanical Alloying and Milling*, Marcel Dekker, New York **2004**.
[45] C.Z. Wu, P. Wang, X. Yao, C. Liu, D.M. Chen, G.Q. Lu, H.M. Cheng, *J. Alloys Compd.* **2006**, 420, 278-282.
[46] S. Rivoirard, P. de Rango, D. Fruchart, J. Charbonnier, D. Vempaire, *J. Alloys Compd.* **2003**, 356–357, 622-625.
[47] R. Floriano, D.R. Leiva, S. Deledda, B.C. Hauback, W.J. Botta, *Mater. Res.* **2013**, 16, 158-163.
[48] A. Patah, A. Takasaki, J.S. Szmyd, *Int. J. Hydrogen Energy* **2009**, 34, 3032-3037.
[49] K.F. Aguey-Zinsou, J.R. Ares Fernandez, T. Klassen, R. Bormann, *Int. J. Hydrogen Energy* **2007**, 32, 2400-2407.
[50] M. Polanski, J. Bystrzycki, *J. Alloys Compd.* **2009**, 486, 697-701.
[51] J.-R. Ares-Fernández, K.-F. Aguey-Zinsou, *Catalysts* **2012**, 2, 330-343.
[52] R. Vujasin, A. Mraković, S. Kurko, N. Novaković, L. Matović, J.G. Novaković, S. Milošević, *Int. J. Hydrogen Energy* **2016**, 41, 4703-4711
[53] S. Milošević, S. Kurko, L. Pasquini, L. Matović, R. Vujasin, N. Novaković, J.G. Novaković, *J. Power Sources* **2016**, 307, 481-488.
[54] K.F. Aguey-Zinsou, J.R. Ares Fernandez, T. Klassen, R. Bormann, *Mater. Res. Bull.* **2006**, 41, 1118-1126.
[55] J. Cui, H. Wang, J. Liu, L. Ouyang, Q. Zhang, D. Sun, X. Yao, M. Zhu, *J. Mater. Chem. A* **2013**, 1, 5603-5611.
[56] R. Floriano, D.R. Leiva, S. Deledda, B.C. Hauback, W.J. Botta, *Int. J. Hydrogen Energy* **2013**, 38, 16193–16198.
[57] G. Liang, J. Huot, S. Boily, a. Van Neste, R. Schulz, *J. Alloys Compd.* **1999**, 292, 247-252.
[58] S. Kurko, Ž. Rašković, N. Novaković, B.P. Mamula, Z. Jovanović, Z. Baščarević, J.G. Novaković, L. Matović, *Int. J. Hydrogen Energy* **2011**, 36, 549-554.
[59] X. Xie, X. Ma, P. Liu, J. Shang, X. Li, T. Liu, *ACS Appl. Mater. Interfaces* **2017**, 9, 5937-5946.
[60] J. Lu, J.C. Young, Z.F. Zhigang, Y.S. Hong, E. Rönnebro, *J. Am. Chem. Soc.* **2009**, 131, 15843-15852.
[61] J. Huot, N. Skryabina and D. Fruchart, *Metals* **2012**, 2 (4), 329-343.
[62] V.M. Skripnyuk, E. Rabkin, Y. Estrin & R. Lapovok, *Acta Mater.* **2004**, 52(2), 405–414.
[63] V.M. Skripnyuk, E. Rabkin, Y. Estrin & R. Lapovok, *Int. J. Hydrogen Energy* **2009**, 34(15) 2009, 6320–6324.
[64] D.R. Leiva, D. Fruchart, M. Bacia, G. Girard, N. Skryabina, A.C.S. Villela, S. Miraglia, D.S. dos Santos & W.J. Botta, *Int. J. Mat. Res.* **2009**, 100, 1739-1446.
[65] M. Krystian, M.J. Zehetbauer, H. Kropik, B. Mingler & G. Krexner, *J. Alloys Compd.* 509 (Suppl 1) **2011**, 449-455.
[66] M.J. Zehetbauer. & R.Z. Valiev in *Nanomaterials by Severe Plastic Deformation*, Wiley VCH, Verlag GmbH, ISBN 3–527–30659-5, **2004**,
[67] H.S. Kim & Y. Estrin, *J. of Mater. Process. Technology* **2005**, 410-411, 285-289.
[68] N.E. Skryabina, V.N. Aptukov, P.V. Romanov & D. Fruchart, *PNRPU Mechanics Bulletin* **2014**, 3, 113-128.
[69] G.K. Williamson & W.H. Hall, *Acta Metall.* **1953**, 1, 22-31.
[70] A. Muralidhar, S. Narendranath, H.S. Nayaka, *J. Magn. Alloy.* **2013**, 1, 336–340.
[71] H.G. Svoboda, F. Vago, *Proc. Mater. Sci.* **2015**, 9, 590–598.
[72] S. Nachev, *Evolution microstructurale et comportement mécanique des composites à base de MgH2 au cours des cycles d'hydruration*, PhD thesis Université Grenoble Alpes, France, theses.fr/223507547, **2015**..
[73] Y. Pang & Q. Li, *Int. J. Hydrogen Energy* **2016**, 41, 18072-18087.
[74] F. Hiura, *Latent hardening in pure magnesium single crystals under Uniaxial Deformation at 298 K*, PhD Thesis, McMaster University, Canada, Materials Science and Engineering, macsphere.mcmaster.ca/handle/11375/9003?mode=full., **2010**.
[75] P. de Rango, Ph. Marty & D. Fruchart, *Appl. Phys. A* **2016**, 122(2), 126-136.
[76] A. Chaise, *Etude expérimentale et numérique de réservoirs d'hydrure de magnésium*, PhD Université J. Fourier, Grenoble, **2008.**
[77] V.N. Aptukov, Perm State University, private communication, **2018**.
[78] L. Popilevsky, V.M. Skripnyuk, Y. Estrin, A.K. Dahle, D. Mirabile Gattia, A. Montone and E. Rabkin, *Int. J. Hydrogen Energy* **2013**, 38(27), 12103-12114.
[79] Y. Estrin., A. Vinogradov, *Acta Mater.* **2013**, 61(3), 782-817.

[80] D.R. Leiva, D. Fruchart, M. Bacia, G.Girard, N. Skryabina, A.C.S Villela, S. Miraglia, D.S. dos Santos, D.S., W.J. Botta, *Int. J. Mat. Res.* **2009**, 100, 1739-1446.
[81] A. Revesz, M. Gajdics, L.K. Varga, G. Krallics, L. Peter & T. Spassov, *Int. J Hydrogen Energy* **2014**, 39, 9911-9917.
[82] T. Hongo, K. Edalati, M. Arita, J. Matsuda E. Akiba & Z. Horita, *Acta Mater.* **2015**, 92, 46–54.
[83] J.L. Soubeyroux, D. Fruchart, A. Mikou, M. Pezat & B. Darriet,. *Mat. Res. Bull.* **1984**, 19, 895-904.
[84] B. Darriet, J.L. Soubeyroux, M. Pezat & D. Fruchart, *J. Less Comm. Metals* **1984**, 103, 1, 153-162.
[85] R.V. Denys, A.B. Riabov, J.P. Maehlen, M.V. Lototsky, J.K. Solberg, V.A. Yartys, *Acta Mater.* **2009**, 57, 3989–4000,
[86] R.V. Denys, A.A. Poletaev, J.P. Maehlen, J.K. Solberg, B.P. Tarasov & V.A. Yartys, *Int. J Hydrogen Energy* **2012**, 37, 5710-5722.
[87] X. Liu, Y. Zhu & L. Li, *J. Alloys Compd.* **2008**, 455, 197–202
[88] X.Q. Tran, S.D. McDonald, Q. Gu & S. Matsumura, *Mat. Res. Soc.*, **2016**, 9, 1316-1327.
[89] Q. Luo, Q.-F. Gu, J.-Y. Zhang, S.-L. Chen, K.-C. Chou & Q. Li, *Nature*, *Scientific Reports* **2015**, 1-14.
[90] C. M. Stander, R. Pacey, *J. Phys. Chem. Solids* **1978**, 39, 829-832.
[91] T. Noritake, M. Aoki, S. Towata, Y. Seno, Y. Hirose, E. Nishibori et al. *Appl. Phys. Lett.* **2002**, 81, 2008-2010.
[92] H. G. Schimmel, G. J. Kearley, J. Huot, F. M. Mulder, *J. Alloys Compd.* **2005**, 404–406, 235-237.
[93] A. J. Du, S. C. Smith, G. Q. Lu, *J. Phys. Chem. C* **2007**,111, 8360-8365.
[94] J. L. Bobet, C. Even, Y. Nakamura, E. Akiba, B. Darriet B. *J. Alloys Compd.* **2000**, 298, 279-284.
[95] L. E. A. Berlouis, E. Cabrera, E. Hall-Barientos, P. J. Hall, S. B. Dodd, S. Morris et al. *J. Mater. Res*. **2001**,16(1), 45-57.
[96] J. G. Novaković, T. Brdarić, N. Novaković, Lj. Matović, A. Montone, S. Mentus, *Mater. Sci. Forum* **2007**, 555, 343-348.
[97] G. Liang, R. Schulz, *J. Mater. Sci.* **2003**, 38, 1179-1184.
[98] J-L . Bobet, E. Akiba, Y. Nakamura, B. Darriet, *Int. J. Hydrogen Energy* **2000**, 25, 987-996.
[99] K. Zeng, T. Klassen, W. Oelerich, R. Bormann, *J. Alloys Compd.* **1999**, 283, 213-224.
[100] W. Oelerich, T. Klassen, R. Bormann, *J. Alloys Compd.* **2001**, 322, L5-L9.
[101] A. J. Du, S. C. Smith, X. D. Yao, G. Q. Lu, *J. Phys. Chem. B* **2005**, 109, 18037-18041.
[102] Y . Song, Z. X. Guo, R.Yang, *Phys. Rev. B* **2004**, 69, 094205.
[103] C. X. Shang, M. Bououdina, Y. Song, Z. X. Guo, *Int. J. Hydrogen Energy* **2004**, 29; 73-80.
[104] T. Vegge, L. S. Hedegaard-Jensen, J. Bonde, T. R. Munter, J. K. Norskov. *J. Alloys Compd.* **2005**, 386, 1-7.
[105] P. Larson, C. M. Araújo, J. A. Larsson, P. Jena, R. Ahuja, *PNAS Appl. Phys. Sci.* **2008**, 105(24), 8227-8231.
[106] B. P. Mamula, J. G. Novaković, I. Radisavljević, N. Ivanović, N. Novaković, *Int. J. Hydrogen Energy* **2014**, 39(11), 5874-5887 ;
[107] N. Novaković, Lj. Matović, J. G. Novaković, I. Radisavljević, M. Manasijević, B. P. Mamula, N. Ivanović, *Int. J. Hydrogen Energy* **2010**, 35(2), 598-608
[108] D. Singh in *Plane waves, pseudopotentials and the LAPW method*, Kluwer Academic, **1994**.
[109] P. E. Blöchl, *Phys. Rev. B* **1994**, 50(24), 17953.
[110] P. Blaha, K. Schwarz, G. K. H. Madsen, D. Kvasnicka, J. Luitz, R. Laskowski, F. Tran and L. D. Marks in *WIEN2k, An Augmented Plane Wave + Local Orbitals Program for Calculating Crystal Properties,* (Karlheinz Schwarz, Techn. Universität Wien, Austria), ISBN 3-9501031-1-2, **2018**.
[111] X. Gonze, B. Amadon, P-M. Anglade, J-M. Beuken, F. Bottin, P. Boulanger et al. *Comput. Phys. Commun.* **2009**, 180, 2582-2615.
[112] N. Troullier and José Luís Martins, *Phys. Rev. B* **1991**, 43 , 1993-2006
[113] R. Car, M. Parrinello, *Phys. Rev. Lett.* **1985**, 55, 2471-2474.
[114] W. Andreoni, A. Curioni, *Parallel Computing* **2000**, 26, 819-842..
[115] N. O. J. Malcolm, P. L. A. Popelier, *Faraday Discuss.* **2003**, 124, 353-363.
[116] R. F. W. Bader in *Atoms in Molecules - a Quantum Theory*, Oxford University Press, Oxford, U.K. **1990**.
[117] P. Hohenberg, W. Kohn, **Phys. Rev. 1964**, 136, B864-B871.
[118] E.R. Johnson, S. Keinan, P. Mori-Sánchez, J. Contreras-García, A.J. Cohen, W. Yang, *J. Am. Chem. Soc.* **2010**, 132, 6498-6506.
[119] J. Contreras-García, W. Yang, E. R. Johnson, *J. Phys. Chem. A* **2011**, 115, 12983-12990.
[120] A. Otero-de-la-Roza, E. R. Johnson, J. Contreras-García, *Phys. Chem. Chem. Phys.* **2012**, 14, 12165-12172.
[121] H. Smithson, C. A. Marianetti, D. Morgan, A. V. Vander, A. Predith, G. Ceder, *Phys. Rev. B* **2002**, 66, 144107.
[122] J. P. Perdew, S. Burke, M. Ernzerhof, *Phys. Rev. Lett.* **1996**, 77, 3865-3868.
[123] R. Yu, P. K. Lam, *Phys. Rev B* **1988**, 37(15), 8730-8737.
[124] R. J. Westerwaal, C. P. Broedersz, R. Gremaud, M. Slaman, A. Borgschulte, W. Lohstroh et al., *Thin Solid Films* **2008**, 516, 4351-4359.
[125] R. Griessen, Lectures, web: http://www.nat.vu.nl/wgriessen/STofHinM/STHM.htm.
[126] N. Ivanović, N. Novaković, D. Colognesi, I. Radisavljević, S. Ostojić, *Int. J. Mod. Phys. B* **2010**, 24, 703-710.
[127] G. Wu, S. Liu, J. Zhang, Q. Li, Y. Wu, K. Chou et al. *Trans. Nonferrous Met. Soc. China* **2009**, 19, 383-388.
[128] G. Wu, J. Zhang, Q. Li, Y. Wu, K. Chou, X. Bao, *Comput. Mater. Sci.* **2010**, 49, S144-S149.
[129] A. J. Du, S. C. Smith, X. D. Yao, G. Q. Lu, *Surf. Sci.* **2006**, 600, 1854-1859.
[130] M. S. Park, A. Janotti, C. G. Van de Walle, *Phys. Rev. B* **2009**, 80, 064102.
[131] S. Kurko, I. Milanović, J. Grbović Novaković, N. Ivanović, N. Novaković, *Int. J. Hydrogen Energy* **2014**, 39(2), 862-867.
[132] J. H. Dai, Y. Song, R. Yang, *Int. J. Hydrogen Energy* **2011**, 36, 12939-12949.
[133] A. San-Martin and F. D. Manchester, *J. Phase Equilibria* **1987**, 8, 431–437.
[134] H. Olijnyk and W. B. Holzapfel, *Phys. Rev. B* **1985**, 31, 4682–4683.
[135] D. S. Sholl, *J. Alloys Compd.* **2007**, 446–447, 462–468.
[136] S. Tao, P. Notten, R. van Santen and a. Jansen, *Phys. Rev. B* **2009**, 79, 1–7.
[137] T. Vegge, *Phys. Rev. B - Condens. Matter Mater. Phys.* **2004**, 70, 1–7.
[138] N. Jacobson, B. Tegner, E. Schröder, P. Hyldgaard and B. I. Lundqvist, *Comput. Mater. Sci.* **2002**, 24, 273–277.
[139] K. Klyukin, M. G. Shelyapina and D. Fruchart, *J. Alloys Compd.* **2015**, 644, 371–377.
[140] K. Klyukin, M. G. Shelyapina and D. Fruchart, *J. Alloys Compd.* **2013**, 580, S10–S12.
[141] X. Tan, L. Wang, C. M. B. Holt, B. Zahiri, M. H. Eikerling and D. Mitlin, *Phys. Chem. Chem. Phys.* **2012**, 14, 10904–10909.
[142] D. Fruchart, P. de Rango, J. Charbonnier, N. Skryabina, M. Jehan. *Nanocrystalline composite for storage of hydrogen*. Patent U.S. 2009/0278086, 12 Nov. 2009.
[143] G. Girard, D. Fruchart, O. Fruchart, S. Miraglia, L. Ortega and N. Skryabina, in *International Symposium 'Metal-Hydrogen Systems. Fundamentals and Applications*', Moscow **2010**, 20.
[144] T. Ma, S. Isobe, Y. Wang, N. Hashimoto and S. Ohnuki, *J. Phys. Chem. C* **2013**, 117, 10302–10307.
[145] P. de Rango, A. Chaise, J. Charbonnier, D. Fruchart, M. Jehan, P. Marty, S. Miraglia, S. Rivoirard and N. Skryabina, *J. Alloys Compd.* **2007**, 446–447, 52–57.
[146] J. Charbonnier, P. De Rango, D. Fruchart, S. Miraglia, L. Pontonnier, S. Rivoirard, N. Skryabina and P. Vulliet, *J. Alloys Compd.* **2004**, 383, 205–208.

[147] M. G. Shelyapina, A. V. Vyvodtceva, K. A. Klyukin, O. O. Bavrina, Y. S. Chernyshev, A. F. Privalov and D. Fruchart, *Int. J. Hydrogen Energy* **2015**, 40, 17038–17050.

[148] H. Jonsson, G. Mills and K. W. Jacobsen, in *Nudged elastic band method for finding minimum energy paths of transitions* (Eds.: B. J. Berne, G. Ciccotti and D. F. Coker), World Scientific Publishing, Singapore, **1998**, pp. 385–404.

[149] G. Henkelman, H. Jónsson, P. Giannozzi, S. Baroni, N. Bonini, M. Calandra, R. Car, C. Cavazzoni, D. Ceresoli, G. L. Chiarotti, M. Cococcioni, I. Dabo, A. Dal Corso, S. De Gironcoli, S. Fabris, G. Fratesi, R. Gebauer, U. Gerstmann, C. Gougoussis, A. Kokalj, M. Lazzeri, L. Martin-Samos, N. Marzari, F. Mauri, R. Mazzarello, S. Paolini, A. Pasquarello, L. Paulatto, C. Sbraccia, S. Scandolo, G. Sclauzero, A. P. Seitsonen, A. Smogunov, P. Umari and R. M. Wentzcovitch, *J. Phys. Condens. Matter* **2000**, 21, 395502-1–19.

[150] C. Wert and C. Zener, *Phys. Rev.* **1949**, 76, 1169–1175.

[151] K. W. Kehr, in *Hydrogen in metals I*. (Eds.: G. Alefeld and J. Völkl), Springer, Berlin Heidelberg **1978**, pp. 197–226.

[152] O. O. Bavrina, M. G. Shelyapina, K. A. Klyukin and D. Fruchart, *Int. J. Hydrogen Energy* **2018**, 43, 17338–17345.

[153] C. Nishimura, M. Komaki and M. Amano, *J. Alloys Compd.* **1999**, 293, 329–333.

[154] S. V Alapati, J. Karl Johnson and D. S. Sholl, *Phys. Chem. Chem. Phys.* **2007**, 9, 1438–1452.

[155] J. L. Bobet, E. Akiba and B. Darriet, *Int. J. Hydrogen Energy* **2001**, 26, 493–501.

[156] S. Nachev, P. De Rango, N. Skryabina, A. Skachkov, V. Aptukov, D. Fruchart and P. Marty, *Int. J. Hydrogen Energy* **2015**, 40, 17065–17074.

[157] W. Zhang, G. Xu, Y. Cheng, L. Chen, Q. Huo and S. Liu, *Dalt. Trans.* **2018**, 47, 5217–5225.

[158] D. R. Leiva, R. Floriano, J. Huot, A. M. Jorge, C. Bolfarini, C. S. Kiminami, T. T. Ishikawa and W. J. Botta, *J. Alloys Compd.* **2011**, 509, S444–S448.

[159] V. Ozolins, E.H. Majzoub, C. Wolverton, *Phys. Rev. Lett.* **2008**, 100, 1355011-1355014.

[160] S. Kurko, B. Paskaš-Mamula, Lj. Matović, J. Grbović Novaković, N. Novaković, *Acta Physica Polonica A* **2011**, 120, 238-241.

[161] D. Chen, Y. M. Wang, L. Chen, S. Liu, C. X. Ma, L. B. Wang, *Acta. Mater.* **2004**, 52, 521-528.

[162] J. H. Dai, Y. Song, R. Yang, *J. Phys. Chem. C* **2010**, 114, 11328-11334.

[163] S. Er, D. Tiwari, G. A. de Wijs, G. Brocks, *Phys. Rev. B* **2009**, 79(2), 024105.

[164] Y. Song, Z. X. Guo, R. Yang, *Mat. Sci. Eng. A* **2004**, 365, 73-79.

[165] T. Vegge, L. S. Hedegaard-Jensen, J. Bonde, T. R. Munter, J. K. Nørskov, *J. Alloys Compd.* **2005**, 386, 1-7.

[166] S. Giusepponi, M. Celino, *Int. J. Hydrogen Energy* **2013**, 38, 15254-15263.

[167] R. W. P. Wagemans, J. H. Van Lenthe, P. E. De Jongh, A. J. Van Dillen and K. P. De Jong, J. Am. Chem. Soc. **2005**, 127, 16675–16680.

[168] C. C. Koch, Nanostructured Mater. **1997**, 9, 13–22.

[169] P. E. De Jongh, R. W. P. Wagemans, T. M. Eggenhuisen, B. S. Dauvillier, P. B. Radstake, J. D. Meeldijk, J. W. Geus and K. P. De Jong, *Chem. Mater.* **2007**, 19, 6052–6057.

[170] K. F. Aguey-Zinsou and J. R. Ares-Fernández, *Chem. Mater.* **2008**, 20, 376–378.

[171] P. Larsson, C. M. Araújo, J. A. Larsson, P. Jena and R. Ahuja, *PNAS* **2008**, 105, 8227–8231.

[172] M. Y. Siretskiy, M. G. Shelyapina, D. Fruchart, S. Miraglia and N. E. Skryabina, *J. Alloys Compd.* **2009**, 480, 114–116.

[173] M. G. Shelyapina and M. Y. Siretskiy, *Phys. Solid State* **2010**, 52, 1992–1998.

[174] M. G. Shelyapina and D. Fruchart, *Solid State Phenom.* **2011**, 170, 227–231.

[175] D.-W. Zhou, P. Peng, J.-S. Liu, L. Chen and Y. J. Hu, *Trans. Nonferrous Met. Soc. China* **2006**, 16, 23–32.

[176] M. G. Shelyapina, D. Fruchart and P. Wolfers, *Int. J. Hydrogen Energy* **2010**, 35, 2025–2032.

[177] M. G. Shelyapina, D. Fruchart, S. Miraglia and G. Girard, *Phys. Solid State* **2011**, 53, 6–12.

[178] M. G. Shelyapina, V. M. Pinyugzhanin, N. E. Skryabina and B. C. Hauback, *Phys. Solid State* **2013**, 55, 12–20.

[179] S. V. Halilov, D. J. Singh, M. Gupta and R. Gupta, *Phys. Rev. B* **2004**, 70, 195117-1–11.

[180] J. F. Pelletier, J. Huot, M. Sutton, R. Schulz, A. R. Sandy, L. B. Lurio and S. G. J. Mochrie, *Phys. Rev. B* **2001**, 63, 052103-1–4.

[181] J. Zhang, D. wu Zhou and J. shui Liu, *Trans. Nonferrous Met. Soc. China* **2009**, 19, 205–209.

[182] X. Ma, S. Liu and S. Huang, *Int. J. Hydrogen Energy* **2017**, 42, 24797–24810.

[183] K. Klyukin, M. G. Shelyapina and D. Fruchart, *Solid State Phenom.*, **2011**, 170, 298–301.

[184] A. Junkaew, B. Ham, X. Zhang, A. Talapatra and R. Arróyave, *Mater. Res. Lett.* **2013**, 1, 161–167.

[185] G. B. Thompson, R. Banerjee, S. A. Dregia and H. L. Fraser, *Acta Mater.* **2003**, 51, 5285–5294.

[186] A. Kumar, I. J. Beyerlein and J. Wang, *Appl. Phys. Lett.* **2014**, 105, 071602-1–5.

[187] B. Ham and X. Zhang, *Mater. Sci. Eng. A* **2011**, 528, 2028–2033.

[188] S. Pathak, N. Velisavljevic, J. Kevin Baldwin, M. Jain, S. Zheng, N. A. Mara and I. J. Beyerlein, *Sci. Rep.* **2017**, 7, 8264:1-9.

[189] H. Hirate, M. Morinaga, H. Yukawa, H. Nakai, *J. Alloys Compd.* **2011**, 509 (Suppl. 2), S612-S615.

[190] K. S. Jung, D. H. Kim, E. Y. Lee, K. S. Lee, *Catal. Today* **2007**, 120, 270-275.

[191] D. L. Croston, D. M. Grant, G. S. Walker, *J. Alloys Compd.* **2010**, 492, 251-258.

[192] H. Yu, S. Zhang, H. Zhao, G. Will, P. Liu, *Electrochim. Acta* **2009**, 54(4), 1319-1324.

[193] S. K. Pandey, A. Bhatnagar, R. R. Shahi, M. S. L. Hudson, M. K. Singh, O. N. Srivastava, *J. Nanosci. Nanotechnol.* **2013**, 13, 5493-5499.

[194] X.-L. Yin, M. Calatayud, H. Qiu, Y. Wang, A. Birkner, C. Minot, Ch. Wöll, *ChemPhysChem* **2008**, 9, 253-256.

[195] P.M. Kowalski, B. Meyer, D. Marx, *Phys. Rev. B* **2009**, 79, 115410.

[196] F. Filippone, G. Mattioli, P. Alippi, A. Amore Bonapasta, *Phys. Rev. B* **2009**, 80, 245203.

[197] R. Vujasin, J.Grbović Novaković, N. Novaković, S.Giusepponi, M.Cellino, *J. Alloys Compd.* 696 **2017**, 548-559.

10.1002/cphc.201801125

WILEY-VCH

REVIEW

This review deals with defects related destabilization methods for improvement of storage properties of some Mg-based hydrides. Theoretical and experimental approaches were used to investigate the influence of various types of defects on structure and stability of hydrides.

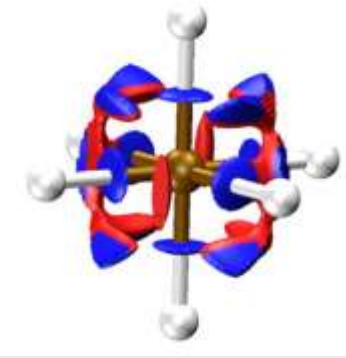

J. Grbović Novaković, N. Novaković, S. Kurko, S. Milošević Govedarović, T. Pantić, B. Paskaš Mamula, K. Batalović, J. Radaković, J. Rmuš, M. Shelyapina, N. Skryabina, P. de Rango and D. Fruchart*

Page No. – Page No.

Influence of defects on Mg-based hydrides stability and hydrogen sorption behavior